UNIVERSITY OF NAIROBI

DEPARTMENT OF PHYSICS

NEW INSIGHTS INTO THE STRUCTURAL, ELECTRONIC, OPTICAL AND PHONON PROPERTIES OF CUBIC AND ORTHORHOMBIC $CsPbI_3$ PEROVSKITE THROUGH FIRST-PRINCIPLES METHOD FOR PHOTOVOLTAIC APPLICATIONS

By

MARTIN ODUOR NYAMUNGA

B.Sc (Physics Major)

I56/38739/2020

A Thesis Submitted in Partial Fulfilment of the Requirements for the Award of the Degree of Master of Science in Physics of the University of Nairobi.

May, 2023

DECLARATION

I declare that this is my original work and has not been submitted in any other University. Where other people's work has been used, this has properly been acknowledged and referenced in accordance with the University of Nairobi's requirements.

Martin Oduor Nyamunga

Signature  Date: 07/09/2023

REG NO. I56/38739/2020

Declaration by Supervisors

This thesis is submitted for examination with our approval as research supervisors:

Signature:  Date: 08/09/2023

Prof. Musembi Robinson,

Department of Physics

University of Nairobi

musembirj@uonbi.ac.ke

Signature:  Date: 08/09/2023

Prof Francis W. Nyongesa

Department of Physics

University of Nairobi

fnyongesa@uonbi.ac.ke

DEDICATION

The project is dedicated to my son Malcolm.

ACKNOWLEDGEMENT

I start by acknowledging God’s greatness, for it is in His wisdom that He bequeathed man with knowledge, skills and wisdom to explore the creation and make life beautiful and meaningful. Next, I want to give a special thank you to Professor Musembi and Professor Nyongesa, whose direction and encouragement allowed me to acquire the necessary computational knowledge and skills to put this work together. My access to CHPC was made possible through the intervention of Prof. Musembi, which made the computational work simpler and quicker. I can't express enough gratitude to my first-year master’s coursework lecturers; Prof. Mwabora, Drs. Okengo, Ogacho, Waita, Nyangonda, and Mureramanzi. Additionally, I want to thank Mwende Mbilo, a PhD student in the Department of Physics, for assisting in training postgraduate students on DFT. Finally, I would like to thank the International Programme on Physical Sciences for the seed funding of computational resources and the Centre for High Performance Computing (CHPC) for giving access to the High-Performance Computing resources through the account; MATS1321.

ABSTRACT

This study has been done using the first-principles technique based on the plane wave self-consistent field method as implemented in the quantum espresso computational code. The GGA has been used as the exchange-correlation potential while the exchange-correlation functionals used in this work are those based on Perdew Burke Ernzerhof (GGA-PBE), and Perdew Burke Ernzerhof for solids (GGA-PBEsol). The other exchange-correlation functionals used were norm-conserving (NC) scalar relativistic type used in calculating the structural, elastic, electronic, phonon-induced thermal stability, and anisotropic optical properties of cubic (α-$CsPbI_3$) and orthorhombic (δ-$CsPbI_3$), with consideration that incident radiation is oriented in the x, y and z directions. For the orthorhombic $CsPbI_3$, the GGA-PBE and GGA-PBEsol with PAW pseudopotentials were also used to calculate the electronic properties. The results showed the following direct band gaps for the orthorhombic structure: 2.4579 eV, 2.321346 eV and 2.39372 eV for GGA-PBE with PAW, GGA-PBE and GGA-PBEsol with NC pseudopotentials, respectively. On the other hand, for cubic structure, the direct band gaps calculated were 1.195219 eV and 1.169895 eV for GGA-PBE and GGA-PBEsol, respectively, with NC pseudopotentials. For the cubic structure, the states that dominated the conduction band are Cs 3(*s*), I 2(*s*), I 3(*p*), and Pb 5(*p*) in the case of GGA-PBE with NC pseudopotentials, and Cs 3(*s*), Pb 3(*p*), I 1(*s*) and I 2(*p*) for GGA-PBEsol with NC pseudopotential. For the orthorhombic structure, the conduction band was dominated by Cs 3(*d*) and Pb 2(*p*) for GGA-PBE with NC pseudopotentials. Pb 3(*p*) and I 2(*p*) dominated the conduction band in the case of PBEsol. The bulk modulus values ranged from 1317 - 1498 kbar for the orthorhombic structure and 159 kbar for the cubic structure. The calculated equilibrium volume and lattice constants for cubic and orthorhombic $CsPbI_3$ agree with the experimental results. Both orthorhombic and cubic structures have been found to have optimal absorptivity within the visible radiation range extending to the edge of the UV radiation, whence the refractive index peaks. The calculated elastic properties depict the cubic structure as flexible. The imaginary phonon frequencies at low temperatures reveal slight structural instability for cubic (α-$CsPbI_3$).

TABLE OF CONTENTS

LIST OF FIGURES

LIST OF TABLES

LIST OF SYMBOLS AND ABBREVIATIONS

CB	Conduction Band
CBM	Conduction Band Momentum
CC	Combined Circle
CHPC	Centre for High Performance Computing
DFT	Density Functional Theory
DOS	Density of States
E_{xc}	Exchange Correlation Energy
GGA	Generalized Gradient Approximation
LDA	Local Density Approximation
LEDs	Light Emitting Diodes
LSDA	Local Spin Density Approximation
NC	Norm-Conserving
PAW	Projector Augmented Wave
PBE	Perdew–Burke–Ernzerhof
PCE	Power Conversion Efficiency
PDOS	Partial Density of States
PV	Photovoltaics
QD	Quantum Dot
QE	Quantum Espresso
TDOS	Total Density of States
USSP	Ultrasoft Pseudopotentials
UV	Ultraviolet
VBM	Valence Band Momentum
$\rho(r)$	Electron Density Function

CHAPTER ONE: INTRODUCTION

1.1 Background of the Study

The price of petroleum has been steadily rising ever since the energy crisis of the 1960s. The primary forms of energy used today are fossil fuels, which have historically been seen as advantageous financially despite having detrimental environmental effects(Albrecht and Rech, 2017). The availability of fossil fuels is finite, and they may eventually run out. Therefore, it is necessary to look for alternate sources of energy. Although silicon-based photovoltaics have been functioning well so far, there is a need to develop a strong alternative material with an equivalent or greater conversion-efficiency at reduced manufacturing costs and long-term stability to stave off the impending scarcity (Killam *et al*., 2017). The need to diversify the energy sources is further compounded by the need to mitigate against climate change (Barkhouse *et al*., 2015). The most recent measurements of conversion efficiency have shown 22.1 percent efficiency for single junction monocrystalline silicon solar cells with an area of 0.0946 cm^2, and 19.7 percent for bigger devices with an area of 0.9917 cm^2 (Barkhouse *et al*., 2015). Table 1.1 displays the estimated prices for different energy sources (Fraas, 2014).

Table 1. 1 Projected costs of electricity from various fuel sources (Fraas, 2014)

Plant type	Range for total system levelized costs (2010 USD/MWh)		
	Minimum	Average	Maximum
Conventional coal	90.1	99.6	116.3
Advanced coal	103.9	112.2	126.1
Advanced coal with CCS	129.6	140.7	162.4
Natural gas fired			
Conventional combined cycle	61.8	68.6	88.1
Advanced combined cycle	58.9	65.5	83.3
Advanced CC with CCS	82.8	92.8	110.9
Conventional combustion turbine	94.6	132.0	164.1
Advanced combustion turbine	80.4	105.3	133.0
Advanced nuclear	108.4	112.7	120.1
Geothermal	85.0	99.6	113.9
Biomass	101.5	120.2	142.8
Wind	78.2	96.8	114.1
Solar PV	122.2	156.9	245.6
Solar thermal	182.7	251.0	400.7
Hydro	57.8	88.9	147.6

O&M = operation and maintenance. *CC* = combined cycle. *CCS* = carbon capture and sequestration. *PV* = photovoltaics. *GHG* = greenhouse gas

Latest evidence shows that increased energy production as well as a shift from silicon-based PV technologies to thin film technologies are accompanied by a decrease in the costs passed down to the consumers (Barron, 2015). Thus, there is a need for robust development of alternative materials whose properties shall meet the demand for future energy generation and a successful shift from pollution-intensive fuels. This is the reason that has necessitated further research into new era of perovskite material technologies in the field of photovoltaics (Tao *et al*., 2019). Perovskites refer to a class of compounds which have the same type of crystal structure as $CaTiO_3$. The optical band gaps of perovskites can be tuned by mixing or exchanging ions in the three APbX (A = Cs, X = I_3) elements. These alterations are made to ensure that in tandem solar cells, there is an overlap between the solar spectrum and band gaps (Tao *et al*., 2019). Light emitting diodes (LED) made from these materials have their emission wavelengths controlled by this band gap tuning (Tao *et al*., 2019) . Both the experimental and computational approaches have been used to characterize the band gaps for both primary and complex mixtures of perovskites. Complex interplay has been observed through combination of different sizes and types of A, B and X ions. Several studies have been done for different perovskite materials to ascertain their electronic and optical bands gaps; For example, the electronic band gap for methylammonium lead iodide ($MAPbI_3$) has been found to lie between 5.1 eV and 6.65 eV, and that for methylammonium tin iodide ($MASnI_3$) ranging between 4.73-5.47 eV. These variations being linked to data evaluation errors and inconsistencies (Tao *et al*., 2019). Silicon-based semiconductors have been widely used in the manufacture of optoelectronic devices (Gibson, 2019); Among them, light emitting diode (LED), photodetectors (photodiodes) and solar cells. The working principle of these silicon-based semiconductors is dependent on their band gap energy as well as the carrier separation in the depletion zone. Silicon has been preferred because of its indirect band gap; however, the process of radiative recombination, which is the basis for the application of photoemitting

devices, is possible if crystal momentum and energy are conserved (Belyakov *et al*., 2008). In this case, the energy of emitted photon must have the energy of the band gap, i.e. the band gap energy, $E_g = hv$. On the other hand, for conservation of crystal momentum to happen, the transition in the bands structure diagram should be vertical, i.e., electron and the hole must have the same crystal momentum (ħk), which is not possible between Conduction Band Momentum (CBM) and Valence Band Momentum (VBM) of silicon due to their different k-vectors (Hoffman *et al*., 2015).

Although silicon is the most common material used for solar cells, its indirect band gap makes it less ideal (Billah *et al*., 2015). Given that there is a theoretical limit to the highest possible photovoltaic device power conversion efficiency (PCE), it is possible to theoretically model, from first principles, materials with higher conversion efficiency limits, through material optimization methods based on density functional theory, DFT. This must be done to realize energy gap sizes that are most suitable for respective applications (Hoffman *et al*., 2015). Because of the importance of band gaps in the applications of semiconductors, recently, attention has been drawn to solution-based semiconductors. Solar energy materials have gone through different epochs of development stages from the early silicon solar cells, thin film solar cells, dye-sensitized, to solution-processed semiconductors with general formula ABX_3; where A and B are cations while X is a halide anion (Kang and Han, 2018). Band gaps of perovskites such as $CsPbCl_3$, $CsPbI_3$ and $CsPbBr_3$ change with changes in lattice basis structure (Maqbool *et al*., 2017). Perovskites have direct band gap and hence absorb both UV and visible light. Perovskites also have narrow band gaps, and hence are good photon absorbers. They also retain the energy they absorb because of their extremely low thermal conductivities(Haeger *et al*., 2020). This retentivity makes them suitable storage and solar cells materials (Maqbool *et al*., 2017). With high incident photon energy these materials become super-luminescent. Findings on the cubic structure of $CsPbI_3$ have depicted a highly luminescent material with a reduced

bandgap (Maqbool *et al*., 2017). While most research works have focused on *ab initio* modelling of $CsPbI_3$ based on dopant materials, this work exploits the tendencies of structural difference and effects on band gaps and effects on their applications thereof. Already, $CsPbI_3$ perovskite has been found to have; flexibility for composition adjustments, tuneable band-gap size, tolerance to defects and highly improved phase stability (Yuan *et al*., 2020).

This study uses DFT approach to model predictions of different structures of cesium lead iodide, with emphasis on cubic and orthorhombic types, generated from projector augmented wave and norm-conserving pseudopotentials, and their corresponding electrical, mechanical, and optical properties, and hence their suitability for photovoltaic applications.

1.2 Statement of the Problem

The growing need to develop more efficient photovoltaic systems, away from the existing silicon-based and organic metal-halide perovskite materials, has triggered several research efforts in the areas of inorganic perovskite solar energy materials. The solar cells are fabricated with several compositional layers each serving a specific purpose in the solar cell, such as the hole transport layer, the light photon absorber layer, and the electron transport layer, as well as the front and back contacts. The properties of these layers need alternative methods of study that are less resource-intensive, and therefore the input of computational tools and approaches are needed to provide an in-depth insight into their behaviour and contribution to the whole solar cell. In this research work, the density functional theory was chosen as the ideal tool to probe into the intrinsic properties of the $CsPbI_3$ at two different lattice structures, that is cubic and orthorhombic. The electronic and optical properties of the orthorhombic lattice structure of $CsPbI_3$ remains understudied as compared to the cubic structure. Similarly, a gap of literature exists for the phonon and anisotropic optical properties of the cubic structure. There is also a

need for an in-depth comparative study of the optical characteristics and polarization-dependence (i.e., anisotropic properties) of both cubic and orthorhombic structures of $CsPbI_3$, based on PBE and PBEsol GGA functionals, while putting into account the shifts in mechanical and electronic properties for each structure.

1.3 Objectives

The main and specific objectives are stated as follows:

1.3.1 Main Objective

The main objective is to determine the effects of lattice structural differences (cubic and orthorhombic) on elastic, electronic, optical and phonon characteristics of $CsPbI_3$ perovskite and assess the consequential suitability for various photovoltaic and optoelectronic applications.

1.3.2 Specific Objectives

a) To study the electronic properties of the cubic and orthorhombic structures of $CsPbI_3$ perovskite materials using different Exchange-Correlation Functionals.

b) To calculate the optical properties, considering the anisotropic polarization-dependence, of cubic and orthorhombic structures of $CsPbI_3$.

c) To determine the elastic and phonon-induced properties, and the consequent thermal stability of each of the structures mentioned in (a) above.

d) To explore the suitability of these material structures for potential optoelectronic and photovoltaic device applications, based on the calculated properties.

1.4 Justification and Significance of the Study

Given that solar radiation manifests random polarizations, most traditional solar cells have been designed to optimize the absorption of radiations irrespective of their directions of polarizations (Batayneh *et al*., 2021). However, it is now evident that materials such as $CsPbI_3$ could absorb incident radiations of different magnitudes depending on the direction of polarization of incident radiation or their inclination angles relative to the incident radiations (Farahat *et al*., 2022). This points to the need to either adopt new solar absorber material or redesign the existing ones for maximum solar capture. This work stems from the earlier research reports that confirm the sensitivity of the anisotropic β-$CsPbI_3$ nanowires to linearly polarized light, and hence their extensive applications in both flexible and rigid substrates (Zhou *et al*., 2018). This study explores the above-mentioned property through the atomicscale modelling and ground-state energy calculations techniques (DFT), a deviation from the traditional experimental methods that would otherwise require intensive resource investments. In addition, to fill the gap of inadequate physical laboratory experimental resources to cover this material, DFT techniques are applied to predict the electronic, elastic and phonon properties of both cubic and orthorhombic properties of $CsPbI_3$. These areas, especially the phonon properties have not been adequately studied for this material.

CHAPTER TWO: LITERATURE REVIEW

2.1 The Evolution of Solar Energy Materials

The growing energy demand has led to search for other alternative sources of energy which are greener such as solar energy harvesting and conversion technologies which include solar fuels, photovoltaics and solar thermal. The Photovoltaic effect, for instance, is a phenomenon first observed and reported by Edmond Becquerel in 1839 and was widely based on a photoelectrochemical process. Globally, a capacity of more than 100 GW of electrical energy is obtained from solar energy conversion systems annually (Gibson, 2019). While the research developments in the 1950s were aimed at expanding applications, and later transformation to commercial technology in the 1980s, the current solar energy technologies are mainly focused on reduction of manufacturing costs as well as production of higher efficiency solar conversion systems. Solar power was integrated into applications such as sensors and portable electronic devices. Further research yielded a new category of photovoltaic devices based on nanotechnology that made it possible for wearable technology as well as devices with in-built solar energy conversion systems (Gibson, 2019).

Light capturing and conversion to electricity by both organic and inorganic materials have seen rapid developments, with a clamour for engineering materials with improved conversion efficiencies. The current research efforts have laid emphasis on solar energy materials with less toxicity, improves radiation absorption coefficients and manipulated grain boundaries to enhance charge-transport with minimal charge-recombination (Green *et al*., 2014). Materials for photovoltaics have evolved from silicon-based, through dye-sensitized to solution-processed organic, inorganic and organic-inorganic hybrid photovoltaic cells. The motivation has been to hit high efficiencies through tandem or stacked architectures and to enable easy integration of systems by assembling on flexible substrates. While it's justified to migrate to perovskite solar cells, it is important to note that nearly 90% of world photovoltaics relies on

some variation of silicon. In addition, around 90% of domestic usage relies on crystalline silicon solar cells. From silicon solar cells of variable crystallinity, through dye-sensitized to perovskites (described by ABX_3; A and B are cations and X is an anion), the current research on solar cells development is majorly focused on material architectures that can easily be fabricated at low costs, yet with strong absorption of solar radiation and high carrier mobility (Green *et al*., 2014). The focus is now progressively shifting to restructuring the perovskites to realize the most suitable band gaps through doping, coating and structural modification (Zhang *et al*., 2021).

2.2 Advances in Perovskite Solar Cells

2.2.1 Cesium Lead Iodide Perovskite

While gains had been made in improving the power conversion efficiency of organic-inorganic hybrid perovskite solar cells to above 23%, their challenging stability and volatile organic components issues motivated further research to develop all-inorganic perovskites ($CsPbX_3$) (Wu *et al*., 2020), where X is a halide (anion) or mixed halides. In this case, X = Cl. Cs is a monovalent cation (Cs^+) while Pb is a divalent metal (Pb^{2+}). A suitable perovskite of excellent radiation absorption and carrier transportation should comprise; a tuneable bandgap, low extinction binding energy and high extinction coefficient (Gourji and Velauthapillai, 2021). The ideal band gap of α-$CsPbCl_3$ is 1.73 eV and 2.82 eV for orthorhombic (non-photoactive) phase. Good quality of films for the perovskite phase of $CsPbI_3$ is achieved after high-temperature complex annealing (Ling *et al*., 2019). The phase transition between $CsPbI_3$ polymorphs is shown in figure 2.1.

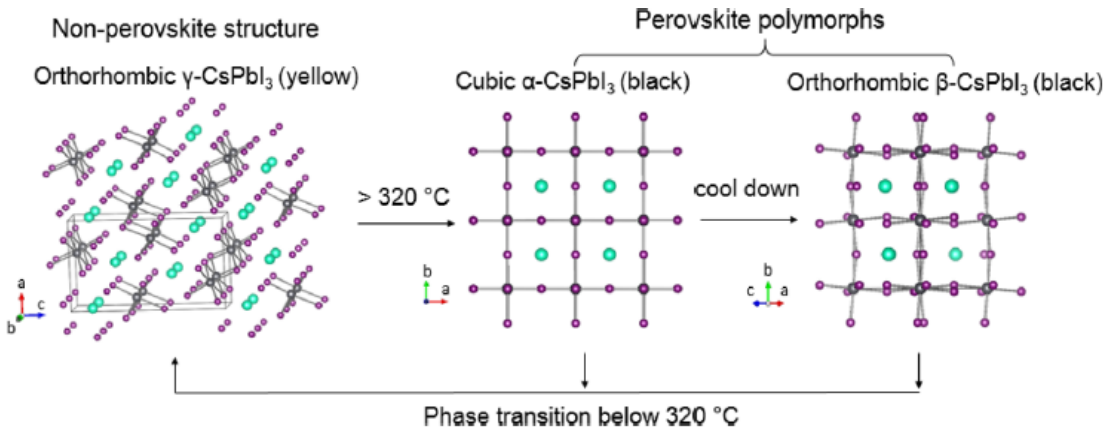

Figure 2.1 Phase transition between polymorphs of $CsPbI_3$ (Ling *et al*., 2019).

While lead (heavy metal) component of the inorganic perovskites has been found to account for the detrimental effects, the focus has been on applying appropriate optimization methods to the metal halides, while taking advantage of the excellent optoelectronic properties of lead to ABX_3 (where B = Pb) because of high symmetry of BX_3 and unique electronic configuration of Pb^{2+} ($6s^2$ $6p^0$), which leads to strong antibonding coupling (Goesten and Hoffmann, 2018). Thus, the focus is on stoichiometric variabilities and their effects on inorganic lead-based halide perovskite.

2.2.2 Perovskite Solar Cell Architecture

Figure 2.2 illustrates the perovskite solar cell structure.

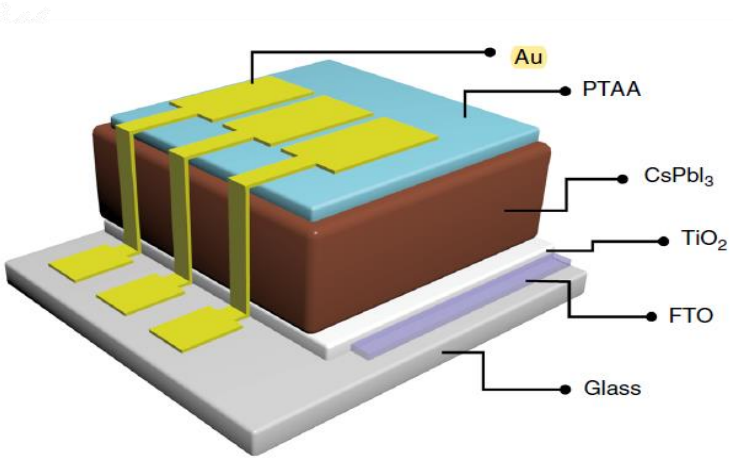

Figure 2.2 Perovskite solar cell device architecture (Gourji and Velauthapillai, 2021).

The cation (Cs^+) component contributes to; decreased temperature of crystallization, enhanced radiation absorption before and after annealing, decreased side phases, improved lifetime of radiation-generated carriers and reduced density of trap states (Gourji and Velauthapillai, 2021).

In the initial attempts to fabricate stable $CsPbI_3$ solar cells, it was observed that the cubic α-$CsPbI_3$, under certain thermal conditions, turns to orthorhombic δ-$CsPbI_3$, which is an undesirable phase. The first fabricated $CsPbI_3$ solar cell had only a maximum power conversion efficiency (PCE) of 2.9% (Green *et al*., 2014). The cubic phase of the resulting structure was stabilized through incorporation of small amounts of hydroiodic acid (HI) to form smaller grains with distorted structure. To achieve higher efficiency, α-$CsPbI_3$ solar cells were fabricated using a new scheme for phase-transition. This yielded a PCE of 4.13%. Further modifications were done to improve PCE to 4.68%, and most recently to 8.80% through vacuum-based vapor deposition (Wang *et al*., 2018). This was succeeded by modification of precursor stoichiometric ratios to achieve about 10.5% efficiency. Achieving stability, however, has remained a challenge (Eperon *et al*., 2015). A more stable form of α-$CsPbI_3$ quantum dots, QDs, of efficiency 10.77% with smaller nano-crystal size was fabricated followed by further adjustment to improve the PCE of α-$CsPbI_3$ QDs to 13.43% through passivation of its surface with a halide salt (F. Li *et al*., 2019).

2.2.3 Mixed Halide Perovskite

Other versions of stable cubic-phase PECs have been made by substituting iodine for bromine. This however, results to widening bandgap (Eperon *et al*., 2015). Even though the hybrid cases, among others, have shown superior responsivity and detectivity to other detectors, they don't retain stability under long-term operation due to lower thermal decomposition temperatures. (Shil *et al*., 2021).

Lower-symmetry perovskites such as γ-$CsPbI_3$ and β-$CsPbI_3$ are more stable due to lower phase-transition temperatures; they have transition temperatures of 175^0C and 260^0C respectively. The α-$CsPbI_3$ (undistorted) has a higher transition temperature of 360^0C, and thus is only stable above this temperature. The lower symmetry perovskites have orthorhombic black phase (Wang *et al*., 2018). When HI (Hydroiodic acid) and PEAI (Phenylethyl ammonium iodide) were incorporated into $CsPbI_3$ precursor solution during the fabrication, a stable and distorted black-phase $CsPbI_3$ with a PCE of 15.07% was obtained. This new material had excellent crystalline structure with efficiency surpassing those reported earlier of similar perovskites (Wang *et al*., 2018). Diagram of phase transition from δ-$CsPbCl_3$ to α-$CsPbCl_3$ is shown as follows (Eperon *et al*., 2015):

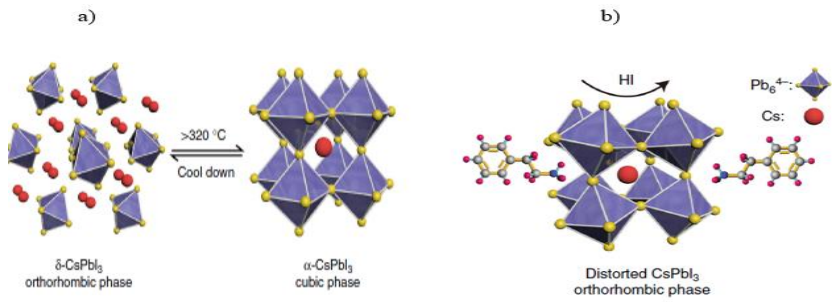

Figure 2.3 a) Diagram of Phase Transition of $CsPbI_3$. b) Orthorhombic Phase of $CsPbI_3$ (Eperon *et al*., 2015).

2.3 Optical Properties and Anisotropy

Calculations of imaginary and real parts of the dielectric function of MoS_2, whose peaks represents inter-band transitions, was done based on different directions of polarization using the Kramer-Kronig relationship, giving a response to incident light depicting a high degree of anisotropy in the infrared regions that ends at the beginning of Ultraviolet (Lahourpour *et al*., 2019). Similar experiments carried out on graphene resulted to JDOS plots for optical inter-band transition peaks in the x, y and z polarization directions, which depicted corresponding band gaps. In this experiment, complex dielectric function ($\varepsilon_{complex} = \varepsilon_1 + i\varepsilon_2$) is used to derive, as a function of frequency, the absorption coefficient, refractive index and reflectivity of

graphene (Alborznia *et al*., 2022). The optical absorption spectra in figure 2.4 were calculated using approximation methods; PBE, HSE06 and TD-HSE06 as represented by the different curves.

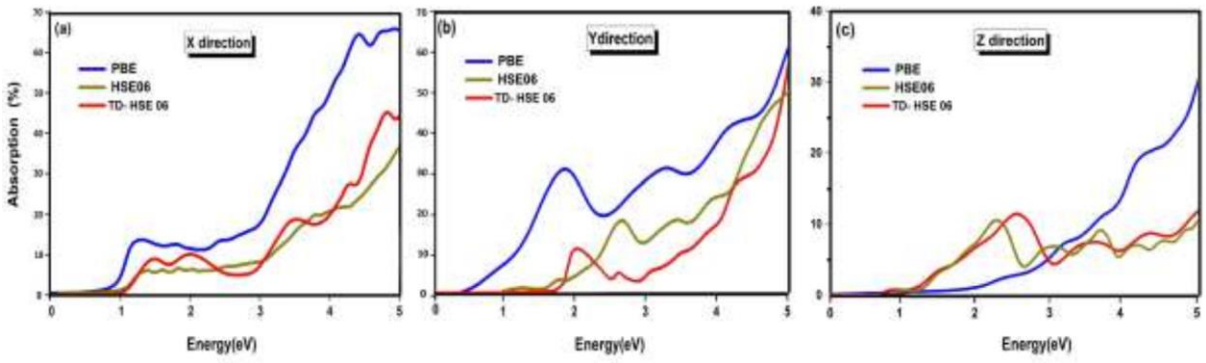

Figure 2.4 In-plane optical absorbance computed with the TD-HSE06 method, HSE06 functional, and PBE functional in X, Y, and Z directions. (Alborznia *et al*., 2022).

In other research performed by (Al Alwash *et al*., 2021), the imaginary parts of the dielectric (see figure 2.6), energy loss, refractive index, reflectivity and absorption coefficient functions were calculated for $CuTaS_3$ in the X, Y and Z directions. The results depict the material as having strong solar absorption characteristics, based on variations in optical parameters in the directions of X, Y and Z polarizations. Different magnitudes of optical absorptions in the Y direction from the X and Z directions, as indicated in figure 2.5, render the material as anisotropic (Al Alwash *et al*., 2021).

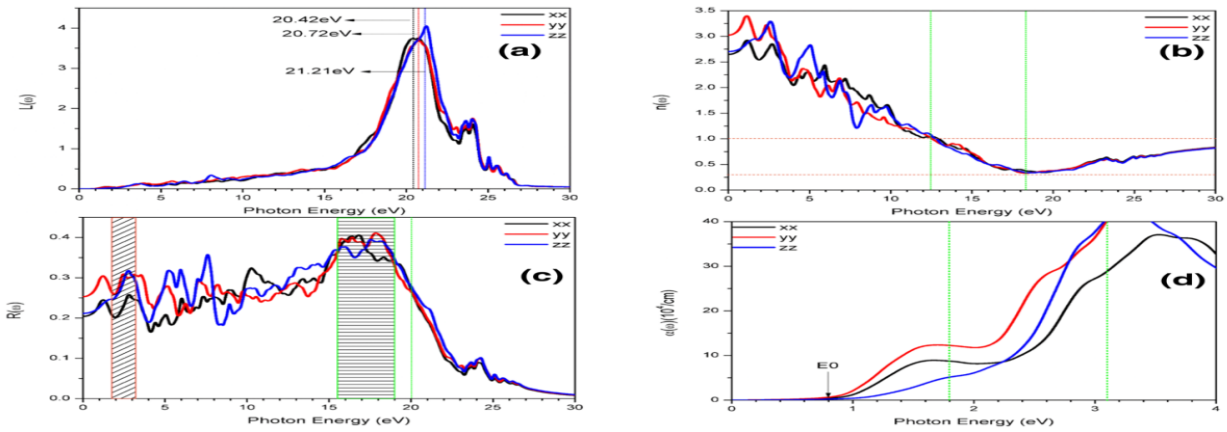

Figure 2.5 Graphs for $CuTaS_3$ of a) Energy loss function, b) Refractive index, c) Reflectivity and d) Absorption coefficient in X, Y and Z directions (Al Alwash *et al*., 2021).

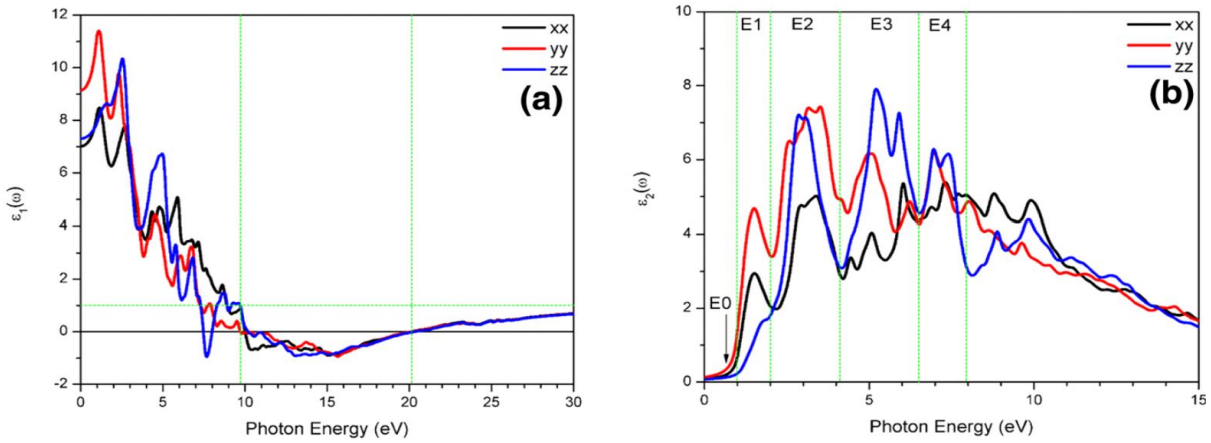

Figure 2.6 Graphs for $CsTaS_3$ showing a) real and b) imaginary parts of dielectric function; incident radiation in the X, Y and Z directions (Al Alwash *et al*., 2021).

Investigations carried out on $CsPbI_3$ using GGA-PBE and mBJ exchange-correlation potential depict direct band gap of 1.72 eV using mBJ, and an absorption coefficient greater than 10^4 cm^{-1} above the bandgap energy, pointing to a good material for photovoltaic applications. Some studies show variations of energy with various optical parameters; refractive index, extinction coefficient, and dielectric function in the GGA-PBE and mBJ comparisons are shown in fig 2.7 (Abhijeet, *et al*., 2021).

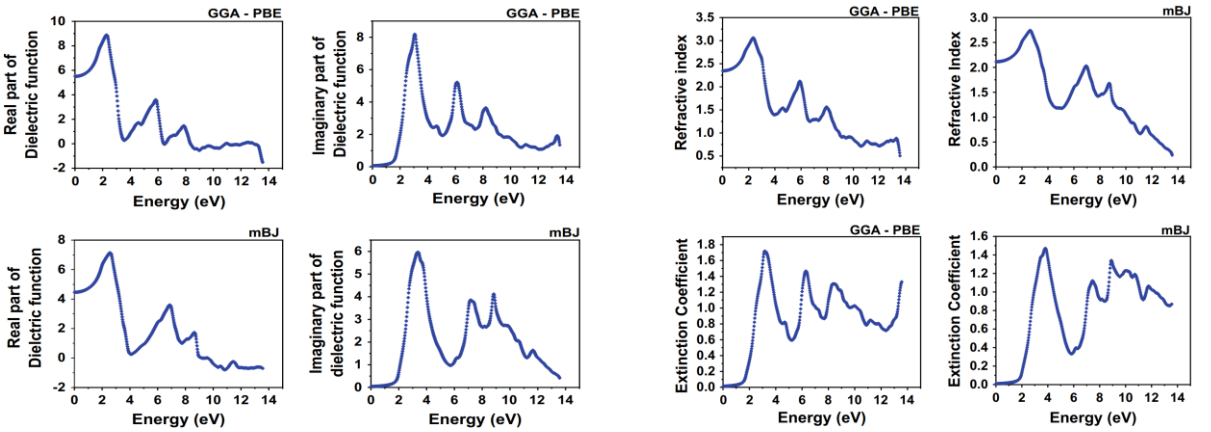

Figure 2.7 Graphs of Dielectric functions computed using the Kramers–Kroning relations. Also shown are the resulting refractive index and extinction coefficient for GGA-PBE and mBJ exchange-correlation potentials (Abhijeet Kale, Rajneesh Chaurasiya, 2021)

Because light signals may be linearly polarized, it is possible to device linearly polarized photodetectors with optical-electrical anisotropic crystal morphology. Polarization direction of

incident radiation changes the absorption of light by materials with one-dimensional structure, e.g. InP, CdSe and $CsPbI_3$ nanowires. These nanowires, when parallel to polarized light, have been found to exhibit stronger sensitivity and absorptivity. High sensitivity is observed from a combination of anisotropic morphology and crystal structure (Zhou *et al*., 2018). The cubic α-$CsPbI_3$ has a symmetric crystal structure, while orthorhombic β- $CsPbI_3$, has an anisotropic structure. α-$CsPbI_3$ has been found to have a band gap of 1.73 eV, suitable for Perovskite solar cells. On the other hand, β- $CsPbI_3$ could either be grown into one-dimensional morphology or, because of their good responsivity, be developed into nanowires for linearly polarized photodetection. This polarization dependence was confirmed experimentally in a Raman-spectra (Zhou *et al*., 2018). A study of TiS_3, whose graph is shown in figure 2.8, was done under different polarizations to determine its optical properties. Several absorption peaks: 2.0 eV, 2.4 eV, 3.0 eV and 3.5 eV depicted its anisotropic properties (Z. Li *et al*., 2020).

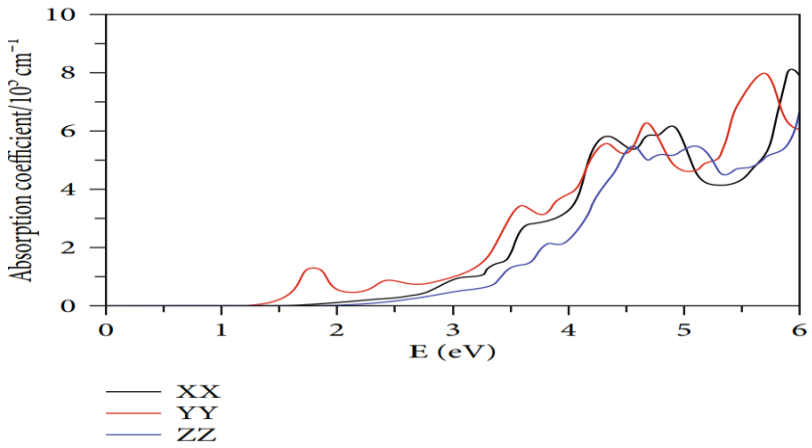

Figure 2.8 Optical absorption coefficients of TiS_3 monolater in the X, Y and Z polarizations (Z. Li *et al*., 2020)

In other findings, MX_3 (M=Ti, Zr; X=S, Se, and Te) as well as ReS_2, are highly anisotropic and possess, because of their low symmetry, exciton absorptivity (Z. Li *et al*., 2020). A time-dependent DFT study of optical properties of cubic $CsPbI_3$ using the GGA-PBE method applied the dielectric function ε(ω) to describe, within defined boundary conditions, the electron-photon interaction for the range of 0-20 eV as shown in figure 2.9. The compound was found

to exhibit transparency between 0 and 2 eV. However, peaks that correspond to optical transitions between VB and CB were observed, indicating high absorptivity of visible radiations. The analysis of the real part indicated the semimetal-metal transition of the material. (Idrissi *et al*., 2021).

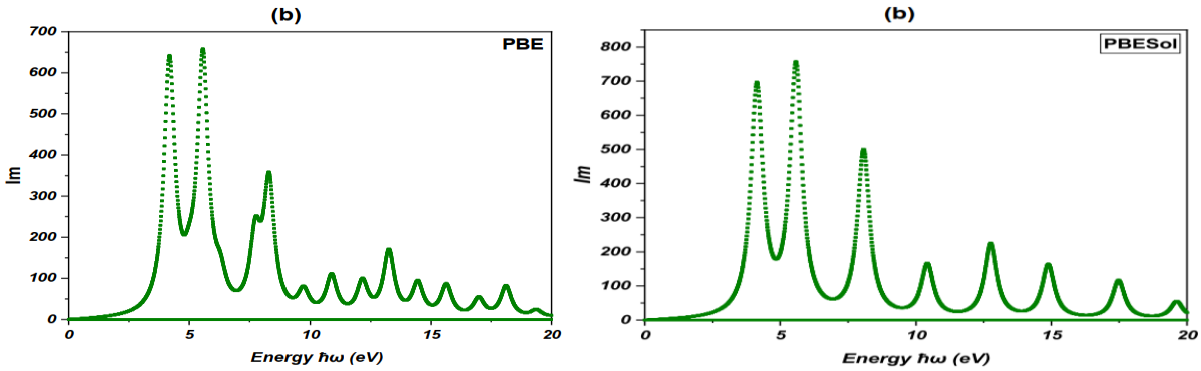

Figure 2.9 TDFT-generated GGA-PBE absorption spectrum of $CsPbI_3$ (Idrissi *et al*., 2021)

2.4 Electronic Properties

Inorganic perovskites have been described as emerging high-efficiency solar harvesting and charge-transporting materials for photovoltaic applications. A percentage power efficiency conversion of about 22.1% has been reported. Improvement in conversion efficiency is being achieved through several methods including adopting better film quality by checking its uniformity and defect passivation and altering optical and electronic properties by tuning material band gap (Meloni *et al*., 2016). Findings of a study on $CsPbI_3$ semiconductor to ascertain its light absorption behaviour showed a band gap of about 1.34 eV in the absence of SOC and a reduced bandgap of 0.20 eV in the presence of SOC (Idrissi *et al*., 2021). It is notable that the bandgap values obtained through DFT calculations are underestimated and may require hybrid functionals for improvement. It is also notable that while using different pseudopotentials such as PBE or mBJ (modified Becke-Johnson) resulting to slightly different bandgap estimates, there are noticeable qualitative similarities (Al-Lehyani, 2021). The near-accurate band gap and projected density of the state of a material can be obtained by first

performing optimization of lattice parameters and position of atoms. The calculated band structure should show whether the bandgap is direct or indirect, which influences the applicability in solar cells (Mbilo *et al*., 2022). Calculations performed on K_4ZnP_2 and K_4CdP_2 and hence the associated plots of PDOS depicted the type of orbitals that dominate the bands, and hence the electronic properties of those materials. Similarly, band energies obtained which are within the UV range showed material's suitability for solar cells (Musembi and Mbilo, 2022).

CHAPTER THREE: THEORETICAL FRAMEWORK

3.1 Density Functional Theory

Density functional theory (DFT) is an approach to a many- body problem used to calculate the electronic structure of a solid-state system by making use of electronic density; a function of three spatial coordinates (Capelle, 2006). The energy of the system is minimized to the ground state in a self-consistent way. The physical properties and electronic structure of real materials are calculated by the ab-initio method. Quantum particles are described using a wave equation given by equation 3.1.

$h = \lambda \cdot p$ (h is the Plank's constant) ……...…… (3.1)

3.2 The Schrödinger Equation

To solve for the electronic structure of a real material, the wave function of an electron must be solved by solving the Schrödinger Equation to obtain the potential field, V (Pranab-Das, 2022). Schrödinger Equation is generally a non-relativistic, single particle system's equation that overlooks effects of gravity and particle interactions. Equation 3.2 represents the linear partial differential equation (the Schrödinger Equation).

$$-\frac{\hbar^2}{2m}\nabla^2\psi(\mathbf{r},t) + V(r,t) = i\hbar\frac{\partial\psi(\mathbf{r},t)}{\partial t} \quad \text{……...……..(3.2)}$$

In solving the Schrödinger Equation, the nucleus is considered heavy and moves slowly as compared to electrons. For the reason of slow relative motion, in a practical sense, the potential field (V) is considered not to be a function of time (t) (Pranab Das, 2022). Equation 3.3 gives the result of separating the spatial and temporal parts of the total wavefunction.

$$\psi(\mathbf{r},t) = \Psi(\mathbf{r})f(t) \quad \text{…….(3.3)}$$

We, therefore, shall not deal with the time-dependent Schrödinger Equation, but time-independent one as shown in figure 3.4. Where $\hbar = \frac{h}{2\pi}$

$$[-\frac{\hbar^2}{2m}\nabla^2 + v(\mathbf{r})]\,\psi(\mathbf{r}) = \varepsilon\psi(\mathbf{r}) \quad (3.4)$$

To calculate the observables, the following expectation values in equations 3.5 and 3.6 are considered (ψ represents a wave function while r represents the position):

$$\langle\psi_i|\psi_j\rangle = \delta_{ij} \quad (3.5)$$

$$\langle\psi_i|\widehat{H}|\psi_i\rangle = \epsilon_i \quad (3.6)$$

A real physical system comprises a huge number of atoms, and thus this becomes a many-body problem whose many-body Schrödinger equation given in equation 3.7 is not easy to solve.

$$[-\frac{\hbar}{2m}\sum_{i=1}^{N}\nabla^2_i + \sum_{i=1}^{N} V(r_i) + \sum_{i=1}^{N}\sum_{j<i} U(r_1, r_2)]\,\psi(r_1, r_2,...,r_N) = E\psi(r_1,r_2,...,r_N] \quad (3.7)$$

It is not practically feasible to obtain exact solutions of an electronic wave function of such a many-body system (N is of the order N^{23}) (Pranab-Das, 2022). For this reason, certain approximations are made to reduce the degree of complexity, which includes with ignoring the dynamics of the ions.

3.3 Hartree-Fock Theory

This is an independent particle model that considers two non-interacting electrons with separable Hamiltonians (Pranab-Das, 2022). Interaction between electrons must be considered, and the wavefunction that describes electron-electron interaction is antisymmetric with-respect-to any set of space-spin coordinates interchange. The wave function which satisfies the condition for anti-symmetry of a two-electron system is given by equation 3.8 (Sholl & Steckel, 2009a).

$$\Psi(\mathbf{r}_1,\mathbf{r}_2) = \frac{1}{\sqrt{2}}[\chi_1(\mathbf{r}_1)\chi_2(\mathbf{r}_2) - \chi_1(\mathbf{r}_2)\chi_2(\mathbf{r}_1)] \quad (3.8)$$

When electrons are presumed to move independently while in the coulombic force field, the Slater determinant, or the antisymmetric product for two electrons is given by equation 3.9:

$$\Psi(\mathbf{r}_1, \mathbf{r}_2) = \frac{1}{\sqrt{2}} \begin{vmatrix} \chi_1(\mathbf{r}_1) & \chi_2(\mathbf{r}_1) \\ \chi_1(\mathbf{r}_2) & \chi_2(\mathbf{r}_2) \end{vmatrix} \quad (3.9)$$

In the case of an N-electron system (where N>2), the resulting Slater determinant is given by equation 3.10:

$$\Psi = \frac{1}{\sqrt{N!}} \begin{vmatrix} \chi_1(\mathbf{r}_1) & \chi_2(\mathbf{r}_1) & \cdots & \chi_N(\mathbf{r}_1) \\ \chi_1(\mathbf{r}_2) & \chi_2(\mathbf{r}_2) & \cdots & \chi_N(\mathbf{r}_2) \\ \vdots & \vdots & \ddots & \vdots \\ \chi_1(\mathbf{r}_N) & \chi_2(\mathbf{r}_N) & \cdots & \chi_N(\mathbf{r}_N) \end{vmatrix} \quad (3.10)$$

The accuracy of the Hartree-Fock method is dependent on the completeness of the expansion basis sets. This model limitation means that an exact solution of the Hartree-Fock equation simply corresponds to an approximate wave function from the Schrödinger equation.

3.4 Hohenberg-Kohn Theorem 1

This theory poses that it is possible to uniquely determine the potential for a given density. The external potential energy v(r) is determined by the ground state density n(r) (Pranab-Das, 2022).

3.5 Hohenberg-Kohn Theorem 2

This Hohenberg-Kohn theorem focuses on solving for the ground state energy by minimizing the total system's energy E(n) instead of solving for a many-electron wave function. This theorem, however, uses approximate functionals of E(n) since the electron density-energy dependence is not explicit in this theorem. To minimize the total energy of the system E(n), electron density n(**r**) must be at the actual ground state (Pranab-Das, 2022). This theorem, however, does not offer practical means of computing the ground-state energy.

3.6 Kohn-Sham Equations

The Kohn-Sham (KS) equations are geared to address the errors of approximation of kinetic energy; they are exact and yield exact density. The Kohn-Sham hypothesis constructs a fictitious system of N non-interacting electrons whose density is approximately equal to that of a physical system. The exact non-interacting K.E (this includes almost all true KEs) is obtained from the solution of the Kohn-Sham equations(Sholl and Steckel, 2009b). The orbitals of the KS system are given by equation 3.11.

$$[-\frac{\hbar^2}{2m}\nabla^2 + v_s(\mathbf{r})]\,\psi_i(\mathbf{r}) = \varepsilon_i\psi_i(\mathbf{r}) \quad \text{(3.11)}$$

The solution to equation 3.11 through equation 3.12 yields equation 3.13.

$$v_s(\mathbf{r}) = v_{ext}(r) + e^2 \int d^3r' \frac{n(\boldsymbol{r})}{\boldsymbol{r}-\boldsymbol{r}'} + v_{xc}(\mathbf{r};[n]) \quad \text{(3.12)}$$

$$n(\mathbf{r}) = \sum_i f_i|\psi(\mathbf{r})|^2 \quad \text{(3.13)}$$

f_i ranges from 0 to 2 and it is the occupational factor of electrons. Ψ_i depends on the external potential (v_{ext}). The problem expressed by equation 3.11 is non-linear and can be solved computationally by first formulating a trial potential which is then iterated to become self-consistent. In this process, owing to the fact that mass of the nucleus is much greater than that of the electron resulting to its slower dynamics, its kinetic energy is ignored. Thus, the KS

wave function of density n(**r**) has the least kinetic energy given by equation 3.14 and yields n(**r**) (Ranasinghe *et al*., 2017). Thus:

$T_s[n] = \langle \Phi[n] | \hat{T} | \Phi[n] \rangle$……..…….……..……..... (3.14)

3.7 Exchange-Correlation Energy Functional

No accurate expression for exchange-correlation ($E_{XC}[\boldsymbol{\rho}]$) has been found so far. The practicality of the DFT calculations would only arise from accurate calculations. However, various approximation methods have been used. These include: LSDA (local spin approximation), LDA (local density approximation), GGA (generalized gradient approximation) and BL3YP (hybrid density functional). The most used approximation methods are LDA and GGA (Pranab-Das, 2022).

3.8 Local Density Approximation (LDA)

LDA divides an inhomogeneous region of electrons into small regions in a system, which is then approximated as homogenous electron gas (Capelle, 2006). Self-consistent calculation (shown in equation 3.15) is performed by the Kohn Sham equation and the Kohn Sham potential (V_{KS}) equation to obtain a non-uniform electron gas exchange-correlation functional using uniform electron gas's density function ρ(r) (Pranab-Das, 2022).

$$E_{XC}^{LDA}[\boldsymbol{\rho}] = \int \rho(\boldsymbol{r}) \varepsilon_{xc}[\rho(\boldsymbol{r})]\, \boldsymbol{dr} \quad \text{……..……..…….……(3.15)}$$

Each particle in a homogenous electron gas has the exchange correlation energy given by $\varepsilon_{xc}[\rho(r)]$. The basis of the exchange correlation potential (LDA) is the local charge density of the system and is suitable for energy bands calculations for semiconductors and metals. It, however, has fallen short in calculating the semiconductor band gaps as well as d-bands of metals (Pranab-Das, 2022).

3.9 Generalized Gradient Approximation (GGA)

Exchange and correlation energies of a system depend on both the density gradient and electron density (Perdew and Yue, 1986). Thus, density gradient and charge density are used to express the exchange-correlation functional as shown in equation 3.16.

$$E_{XC}[\rho] = \int \boldsymbol{\rho}(\boldsymbol{r})\, \varepsilon_{\mathrm{XC}}(\boldsymbol{\rho}(\boldsymbol{r}))\boldsymbol{dr} + \mathrm{E}_{\mathrm{XC}}^{\mathrm{GGA}}(\boldsymbol{\rho}(\boldsymbol{r}), \nabla\boldsymbol{\rho}(\boldsymbol{r})) \quad (3.16)$$

GGA framework is used to develop functionals; PBE, RPBE and PW91 (Chen *et al*., 2020).

3.10 Iteration Scheme's Flow Chat

Figure 3.1 illustrates the process of achieving self-consistency, starting with guessed density.

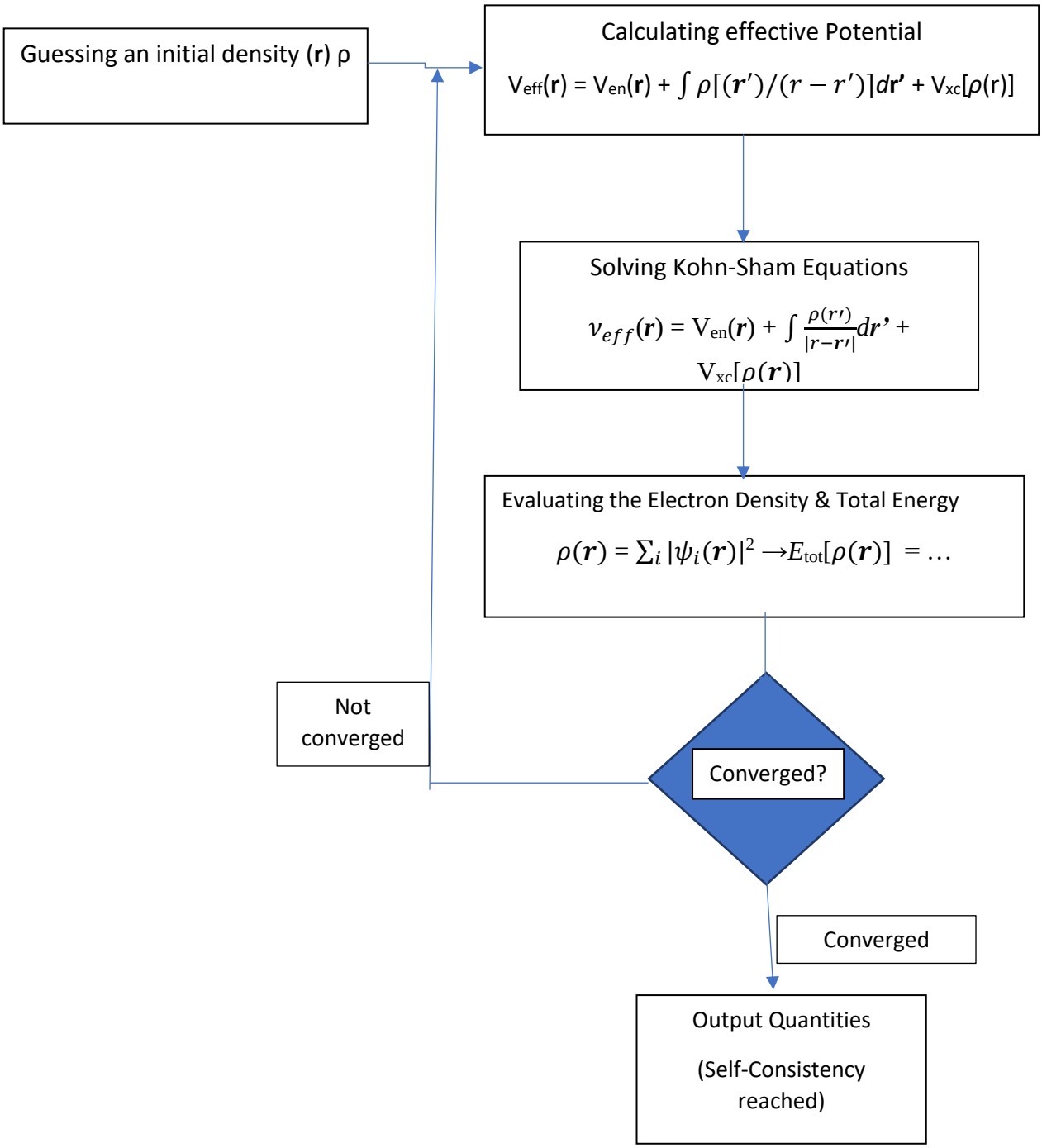

Figure 3.1 Flow chat of iteration scheme (Pranab-Das, 2022).

As shown in fig 3.1, the calculation of $v_{eff}(\boldsymbol{r})$ follows an initial guess for the electron density. Then follows the diagonalization of the Kohn-sham equations and the evaluation of the resulting E_{tot} and $\rho(\boldsymbol{r})$. When the creterion for convergence is not fulfilled, the last $\rho(\boldsymbol{r})$ is

used to continue the numerical process and not the initial guess. The satisfaction of the creterion is followed by computation of various output quantities. The process of achieving self-consistency starts by constructing a pseudo potential for the nucleus using a guessed electron density n(***r***). This yields the Hamiltonian (H^{KS}). Kohn Sham equations are solved to obtain ψ_i (***r***) and n(***r***) which are further iterated to achieve self-consistency. Pseudo potentials are chosen to replace potentials resulting from ions; this removes any oscillations around the core of an atom, hence achieving a reduction of the number of plane wave basis vectors required to make simulation of exact behaviour possible. The constructed pseudo potential shall be contained in a potential file. The approximate solutions obtained shall be compared to the exact experimental results.

CHAPTER FOUR: COMPUTATIONAL METHODS AND MATERIALS

4.1 Equipment and Software

The equipment and software's used in performing the computational work were a laptop with four processors (6 Gb RAM) and virtual machine installed on Hyper-V Manager with two allocated processors. In the virtual machine, Ubuntu Linux distro was installed and thereafter, several software used alongside the computation software were installed such as gfortran, mpich, gnuplot, gcc, etc. The computation software installed were quantum espresso, thermo_pw, and Wannier90. The visualization software installed were: Xcrysden and VESTA, while the graphing tools were gnuplot, excel and Origin. Jobs were prepared in form of input files based on text editor and then submitted to the high-performance computing centre at the Lengau cluster in Cape Town, South Africa.

4.2 Computational Work

All the calculation were done by plane wave self-consistent field, PWscf, method using density functional theory, DFT, as it is implemented in Quantum Espresso (QE) computational code. The generalised gradient approximation was chosen as the exchange correlation potential and the pseudopotentials chosen were the norm conserving scalar relativistic Perdew Burke Ernzerhof and Perdew Burke Ernzerhof for solids, other pseudopotentials used were the projector augmented wave type, PAW. The crystallographic information file (cif) for the material was obtained from materials project, a cloud-based database for materials, then, the cif was processed for further use using the material cloud crystal structure processing tools. Several input files were prepared for self-consistent calculation, non-self-consistent calculations, electronic structure calculations, mechanical properties calculations and optical properties calculations.

4.3 Input file

The input files were prepared for different perovskite structures which comprised the following cards and flags:

- &CONTROL- here we specified the calculation (e.g., scf and nscf), output and pseudodirectory, prefix showing the format of output file storage e.g., 'pwscf'.
- &SYSTEM- under this card were flags that specified the type of Bravais lattice, cell dimensions, number of atoms, cut off energy for wave function and density, type of atoms, DFT methods (e.g., LDA, PBE, RPBE etc.) and occupations among others.
- &ELECTRONS- gave the convergence threshold for self-consistency as well as mixing of densities.
- ATOMIC SPECIES- Under this, we listed the present elements, atomic weight and pseudopotential file. The pseudopotential files consistent with the input DFT were downloaded free from the QE websites and saved at the pseudo-dir.
- ATOMIC POSITIONS- this is the coordinate system of atoms.
- K_POINTS- this was set considering the direction of periodicity that satisfied the convergence.

4.4 Pseudopotentials

The actual ion-electron interactions were replaced with pseudopotentials to eliminate core electrons (rigid core approximation), so that only the electrons that contribute to the materials' chemical properties (valence electrons) are considered. To reduce the number of plane wave basis used in wavefunction expansion, a smoother wave function, whose property simulates the potential field far away from the atomic core, was used. This replaced the changing potential field near the atomic core. For increased efficiency of computation, pseudopotentials

were chosen putting into account their corresponding recommended ecutwfc values from libraries, such as quantum espresso website, that replicated the physical properties of different $CsPbI_3$ perovskites structures. The quantum espresso code was used to compute the convergence against ecutwfc for each structure (cubic and orthorhombic).

4.5 Self-Consistent Calculations and Convergence Testing

The Kohn-Sham equation was solved using input files by performing self-consistent calculations. Mandatory namelists and input cards were specified. Convergence tests were carried out by running calculations using automated scripts in gnuplot to plot total energy against the following parameters: cell parameters, k-points and cut-off energies. Optimal values for conv_thr, eigen values, cut-off energy and stress for vc-relax calculation were factored in for iterations followed by gradually lowering the threshold. The plotting tools used were: gnuplot, excel and Origin.

4.6 Calculations

Input files were created and sent to specified directories in the CHPC, upon which commands for the calculations were ran through the terminal. The calculation process began with relaxation to optimize lattice constants, followed by scf and nscf calculations. This process culminated in the calculation and plotting of bands, DOS, PDOS, elastic and phonon properties. Plottable values for band graphs were obtained using the postprocessing tools: bands.x and plotband.x, while PDOS calculations were done using the projwfc.x code. Graphs were either plotted using gnuplot, Origin or excel graphical tools.

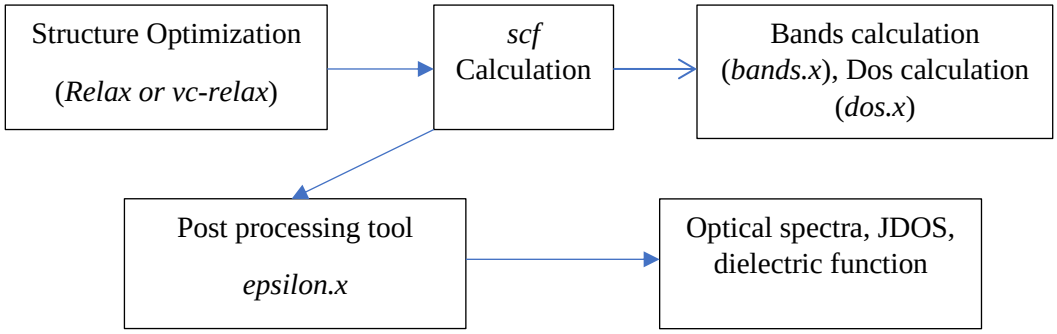

Figure 4.1 Band Structure Calculation Process

4.7 Convergence Tests

4.7.1 Input files preparation

Before convergence testing, an input file was prepared for scf calculation (solving Kohn-Sham equation self-consistently). Norm-conserving pseudopotentials were used in the calculations with a mixing beta value 0.7 for both cubic and orthorhombic $CsPbI_3$. However, in one case, PAW pseudopotentials were used in the calculations for orthorhombic structure. This material was considered a semimetal, and therefore smearing term and degauss were introduced. For better accuracy while maintaining a higher computational speed, the convergence threshold for all the three cases was set at 1.0×10^{-8}.

4.7.2 Convergence against cut-off energy

Cut-off energy of the system was obtained using an automated script by calculating and plotting graphs of total energy of $CsPbI_3$ against various values of ecutwfc. The aim was to obtain ground state energy given in equation 4.1.

$$E_0 = \langle \Psi_0[n_0] | \hat{T} + \hat{U} + \hat{V}_0 | \Psi_0[n_0] \rangle = E[n_0] \quad \text{.....(4.1)}$$

4.7.3 Convergence against k-points

Convergence testing against k-point was done to calculate a finite number of points (k-points) in the Monkhorst-Pack mesh for 2-D $CsPbI_3$. Equal number of sparse, even automatic k-point grid of 7x7x7 with PBE pseudopotential, and sparser k-point grid of 5x5x5 with PBEsol were used in Brillouin zone integrations. Both calculations were performed within specified energy cut-offs (70 and 50 eV respectively) by running PBS scripts.

4.7.4 Convergence against Lattice Constant

This made use of energy cut-off and k-point convergence values calculated earlier. In this case, total energy of the system was computed at different volumes/parameters. The corresponding total energy, shown in equation 4.2, and cell parameters were recorded and plotted using gnuplot. For exactness, the energy and cell dimension values obtained were fitted into the Birch-Murnaghan equation of state. The optimal lattice parameter obtained from ev.x is like that which would be extracted from a parabola plotted from energy-lattice constant graph. Also obtained were the equilibrium volume and bulk modulus of the system.

$$E(V) = E_0 + \frac{9V_0B_0}{16}\left\{\left[\left(\frac{V}{V_0}\right)^{2/3} - 1\right]^3 B_0' + \left[\left(\frac{V}{V_0}\right)^{2/3} - 1\right]^2 \left[6 - 4\left(\frac{V}{V_0}\right)^{2/3}\right]\right\} \quad \text{……...…….(4.2)}$$

4.8 VC-relaxation and scf Calculations

The structures were relaxed using variable cell relaxation method, where the inter-atomic forces were minimised whilst optimizing the overall lattice geometry by minimizing their corresponding potential energy alongside stress tensor components.

4.9 Bands and PDOS Calculations

The bands were calculated from the electron density and potentials computed in the earlier steps. Automatic k-points were used to determine Kohn-Sham eigen values and functions using pw.x program. This was followed by bands calculation using pw.x program and a post-processing tool, bands.x. The bandgap was extracted from the graph.

For PDOS calculation, projwfc.x code was used to calculate the contributions of each atom and orbital (s, p and d orbitals) to valence and conduction bands. The calculations were done for scf followed by nscf with denser k-points. Given multiple s, p and d orbitals, the code sumpdos.x was applied to sum up the contributions of each atom and orbital.

4.10 Optical Calculations

A set of optical parameters; real and imaginary parts of the dielectric tensor diagonal components as a function of frequency, electron energy loss spectrum obtained from the diagonal elements of dielectric tensor and the diagonal components of dielectric tensor were calculated using the imaginary part using the Kramers-Kröning relationship. These results were used to calculate reflectivity, absorption coefficient, refractive index and extinction coefficient.

4.10.1 Dielectric constant

This calculation of the ratio of permittivity of a substance to permittivity of free space begins with self-consistent calculation with some inclusions; nosym = .true., noinv = .true. and !nbnd =500. The former two were used to turn off automatic k-points reduction because crystal symmetries are not recognized by the code epsilon.x. Therefore, the entire k-point list in the grid was included in the calculation.

4.10.2 Refractive Index

Refractive index was calculated from real and imaginary components of dielectric constant ($\sqrt{\varepsilon}$) as shown in equation 4.3.

Where $\varepsilon = \sqrt{\varepsilon}_r + \sqrt{\varepsilon}_i$. Deriving refractive index (n) gives:

$$n_r = \sqrt{\left(\frac{\sqrt{\varepsilon_i^2+\varepsilon_r^2}}{2} - \frac{\varepsilon_r}{2}\right)}$$

$$n_i = \sqrt{\left(\frac{\sqrt{\varepsilon_i^2+\varepsilon_r^2}}{2} + \frac{\varepsilon_r}{2}\right)} \quad \text{.....(4.3)}$$

Where n_r and n_i are real and imaginary parts of refractive index respectively. The result of the calculation was plotted against photon energy.

4.10.3 Extinction Coefficient and Reflectivity

Extinction coefficient, given in equation 4.4, is a measure of absorption of light by a material. Was obtained from real and imaginary dielectric functions. Reflectivity given by equation 4.5 is the amount of light that a body reflects when incident light falls on it.

$$k(\omega) = \left(\frac{1}{\sqrt{2}}\right)\sqrt{\{-\varepsilon_1(\omega) + \sqrt{[\varepsilon^2{}_1(\omega) + \varepsilon^2{}_2(\omega)]}\}} \quad \text{.....(4.4)}$$

$$\text{Reflectivity, } R(\omega) = \frac{(n-1)^2 + k^2}{(n+1)^2 + k^2} \quad \text{.....(4.5)}$$

4.10.4 Absorption Coefficient

This is a calculated ratio of light absorbed to the thickness of the material. It determines the depth of light penetration before it is absorbed.

$$\alpha(\omega) = 4\pi k\varepsilon/(hc/E) \quad \text{.....(4.6)}$$

Given the absorption coefficients were calculated along x, y and z directions. The resolved coefficient was determined using the formular $\alpha = \sqrt{\alpha_x^2 + \alpha_y^2 + \alpha_z^2}$. The coefficients in x, y

and z polarizations were calculated on excel sheets for all values of dielectric constant as well as extinction coefficient.

4.10.5 Optical properties dependence on x, y and z directions

Real and imaginary parts of dielectric constant, refractive index, reflectivity, and absorption coefficient are expressed in x, y and z directions, giving different or, in some cases, nearly similar results. Calculations along all planes were done on excel sheet and results plotted using either gnuplot or excel graphical tool.

CHAPTER FIVE: RESULTS AND DISCUSSION

5.1 Structural Properties

5.1.1 Orthorhombic and cubic crystal system of $CsPbI_3$

Fig 5.1 shows the crystal system of a three-dimensional orthorhombic structure of $CsPbI_3$ from CIF file as generated and visualized on materials project.

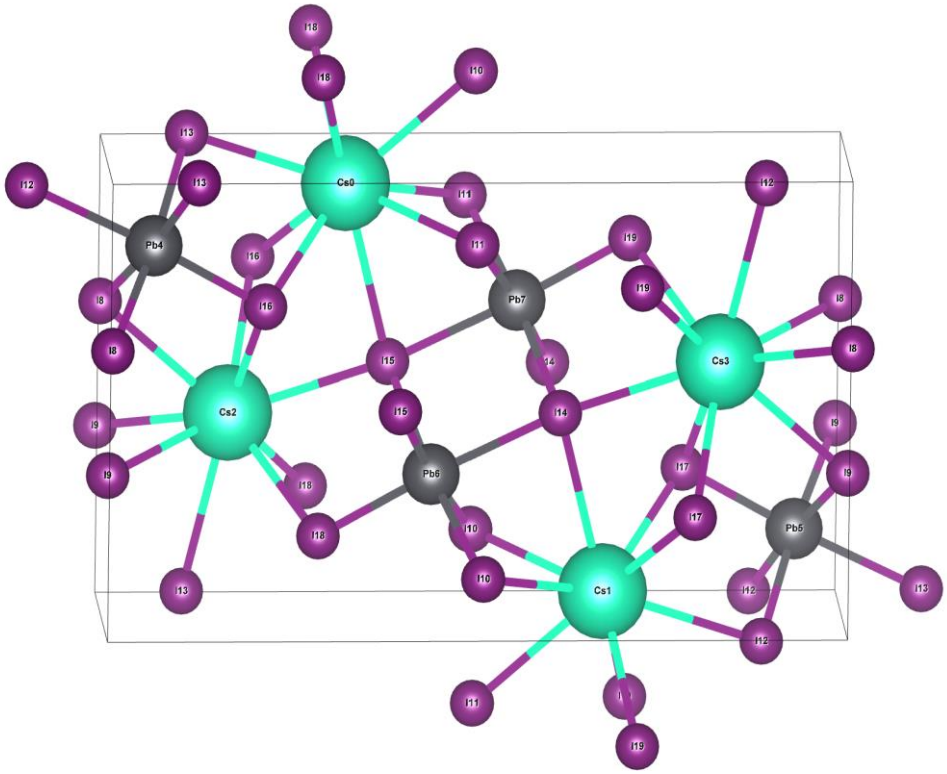

Figure 5.1 Crystal System of Orthorhombic structure of CsPbI3 (Jain *et al*., 2013)

This is a stable, non-magnetic material with a density of 4.98 g/cm^3 and belongs to the space group Pnma and point group mmm. It has bond angles of $\alpha = 90^o$, $\beta = 90^o$ and $\gamma = 90^o$. Lattice parameters before relaxation were:

a = 4.879 Å, b = 10.812 Å, c = 18.213 Å.

5.1.2 Structure Relaxation

Structure optimization for orthorhombic with GGA-PBE (PAW) pseudopotential yielded a graph of total energy against k-points, cut-off energy and cell dimension as shown in figure 5.2 (a), (b) and (c).

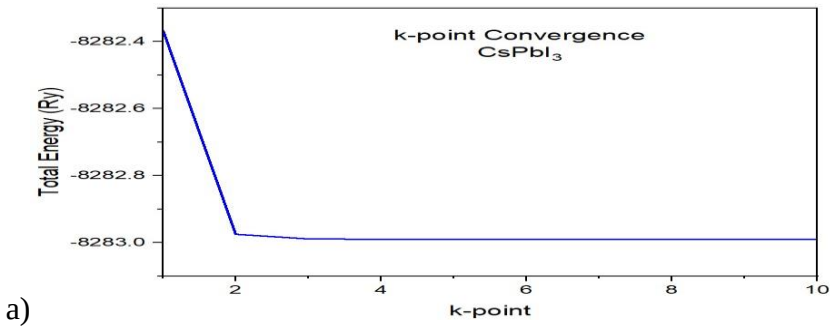

a)

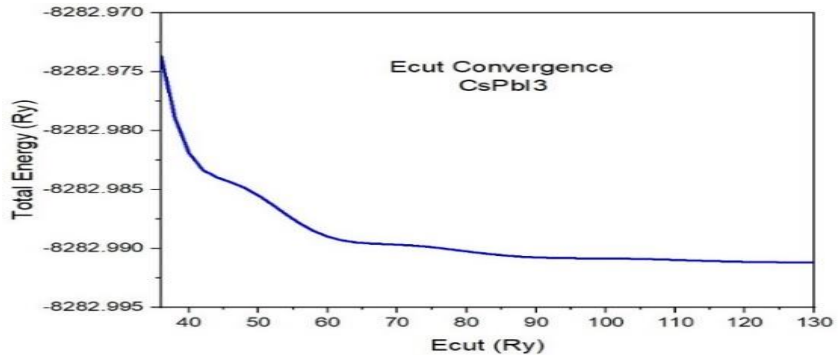

b)

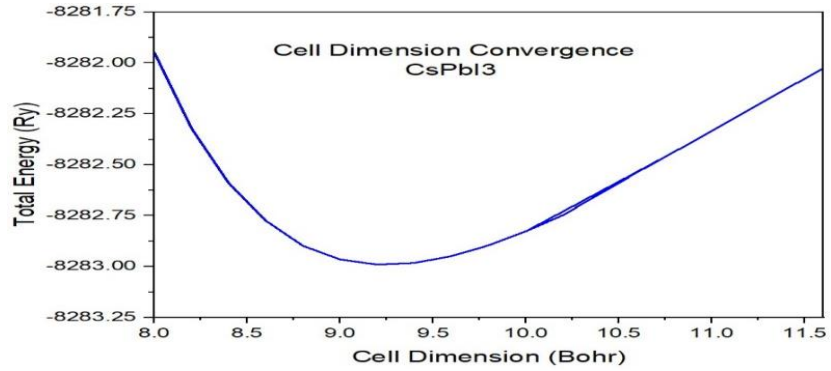

c)

Figure 5.2 Structural parameters a) k-points convergence, b) cut-off energy, c) cell parameter. All are calculated based on GGA-PBE for PAW (PAW-PBE: Projector Augmented Wave method)

The energy and lattice parameters for the orthorhombic $CsPbI_3$ were fitted into the Birch-Murnaghan equation of state by running the code ev.x. The results were:

Lattice parameter a_0 = 9.2272 a.u., Bulk modulus k_0= 1235 kbar, emin = -8282.97482 Ry, Equilibrium cell volume = 785.61 $(a.u.)^3$. The results of the curve fitting were expressed in a smooth Energy-Cell-parameter curve as shown in fig 5.2 (c). BFGS geometry optimization was also performed through variable cell relaxation, vc-relax to relax all the cell parameters. The resulting interatomic force was lowered below 10^{-4} Ry/Bohr, energy below 2.0 x 10^{-4}Ry while the pressure was below 5.0 x 10^{-1}kbar. Vc-relax was used in anticipation for phonon calculations with relaxed structure. The relaxed system at accuracy of 1.3 x 10^{-13} yielded a final enthalpy of -8282.99 Ry, density of 4.95 g/cm^3 and a new cell volume of 6524.43 $a.u.^3$.

When the pseudopotentials were replaced, for this orthorhombic material, with norm-conserving pseudopotentials based on GGA-PBE approximation, the graphs in fig 5.3 were plotted for k-point, kinetic energy cut-off and cell dimension convergence respectively:

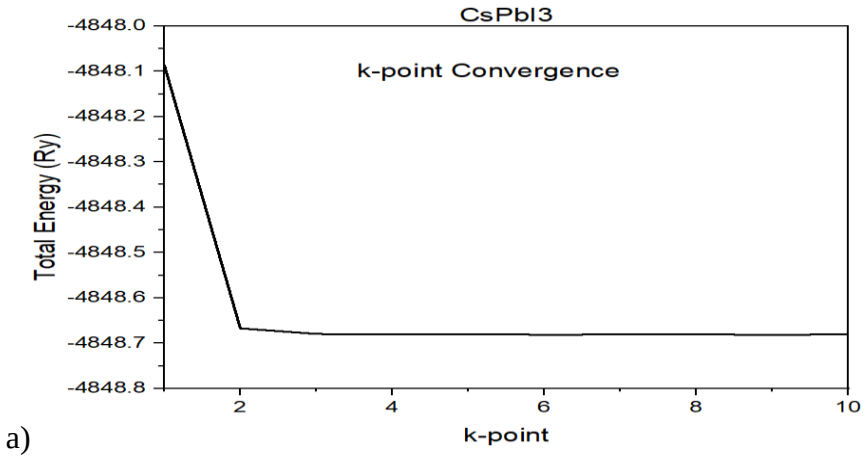

a)

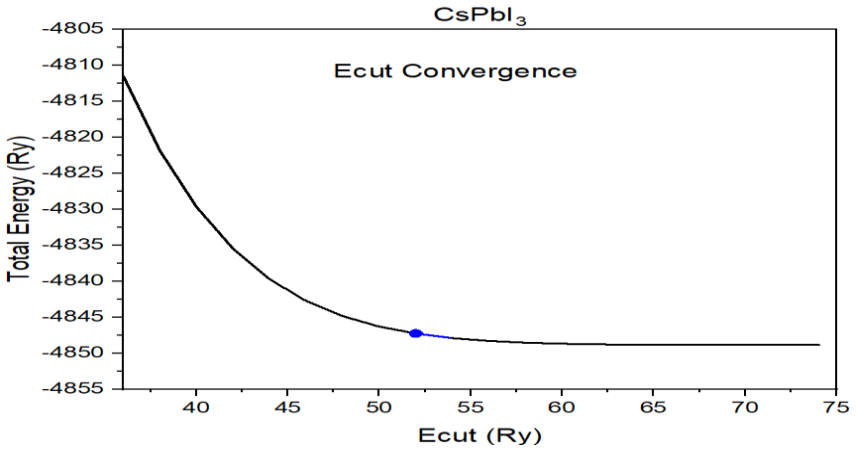

b)

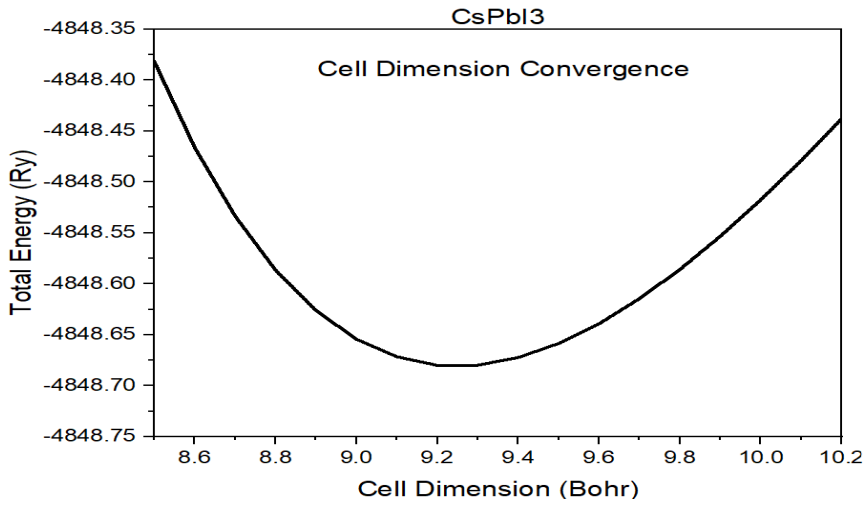

c)

Figure 5.3 Convergence graphs for orthorhombic $CsPbI_3$ a) k-points convergence, b) cut-off energy and c) cell parameter; calculated based on GGA-PBE functional with norm-conserving pseudopotentials.

Fitting the energy and cell parameter values into Birch-Murnaghan equation of state yielded: equilibrium lattice parameter a_0 = 9.2493 a.u., Bulk modulus k_0= 1317 kbar, emin = -4848.67933 Ry and equilibrium cell volume, V_0 = 791.27 $(a.u.)^3$. BFGS convergence done through vc-relax produced: energy < 2.0 x 10^{-04} Ry, force < 1.0 x 10^{-04}Ry/Bohr and cell < 5.0 x 10^{-01}kbar. The final enthalpy of the system was found to be -4848.7899466093 Ry. Other relaxation results are: new unit-cell volume = 5847.22236 $a.u.^3$, density = 5.52563 g/cm^3 and Fermi energy = 6.3599 eV. The relaxed cell parameter, celldm (1) = 8.9358598881 a.u. (close to the result from the curve in fig 5.3 (c). Similar procedure was done for GGA-PBEsol approximation technique giving the results as shown in figure 5.4.

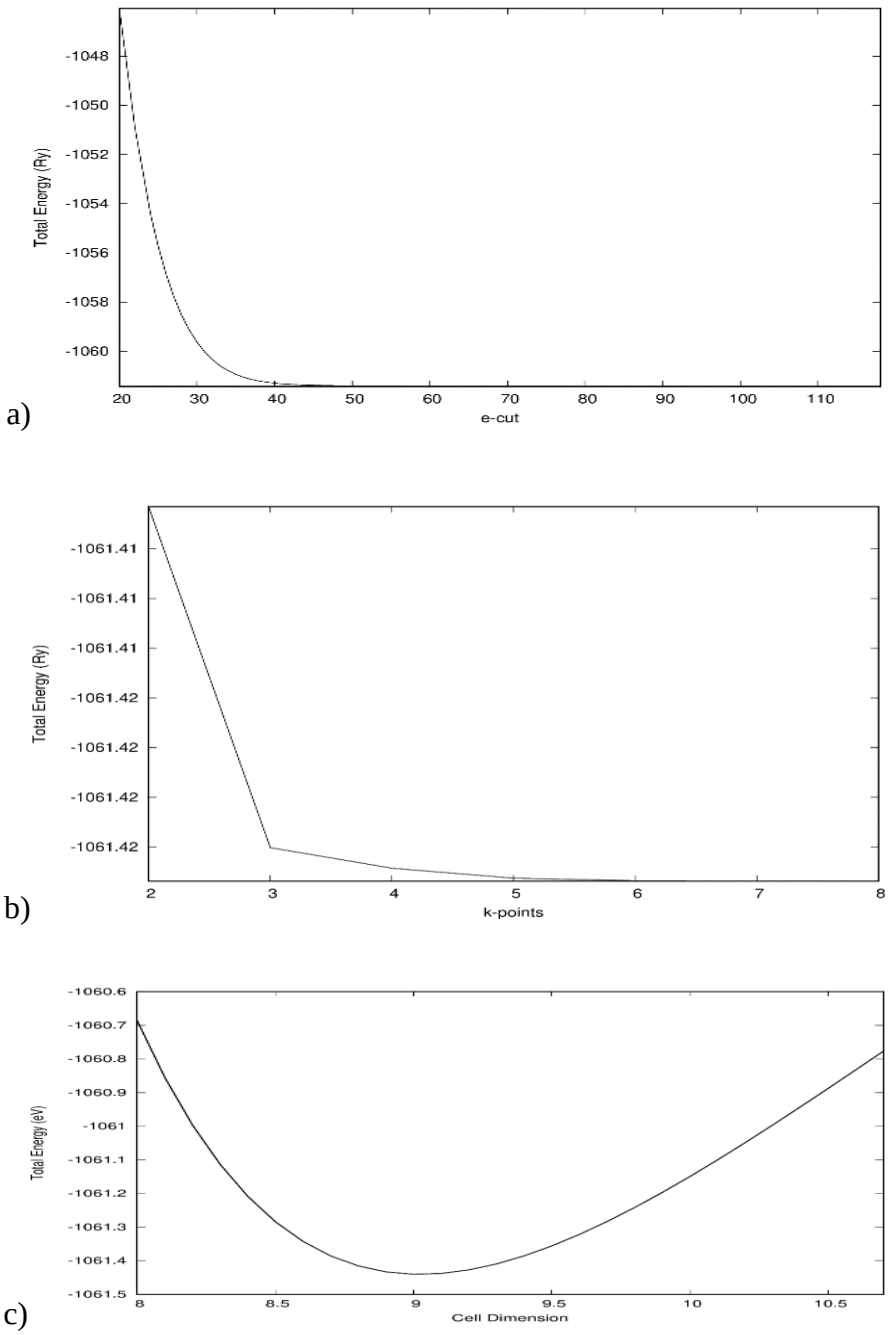

Figure 5.4 Convergence graphs for orthorhombic $CsPbI_3$ plotted based on GGA-PBEsol; a) k-points, b) cut-off energy and c) cell parameter convergence.

Computation was also carried out for cubic crystal system of $CsPbI_3$ with material ID 1069538 and point group $m\bar{3}m$ generated and visualized on materials project. Both GGA-PBE and GGA-PBEsol pseudopotential were used. The cell parameter for the un-relax crystal structure was 6.41Å with bond angles of 90.0^o and volume of 263.89 $Å^3$. Figure 5.5 shows the crystal structure of cubic $CsPbI_3$.

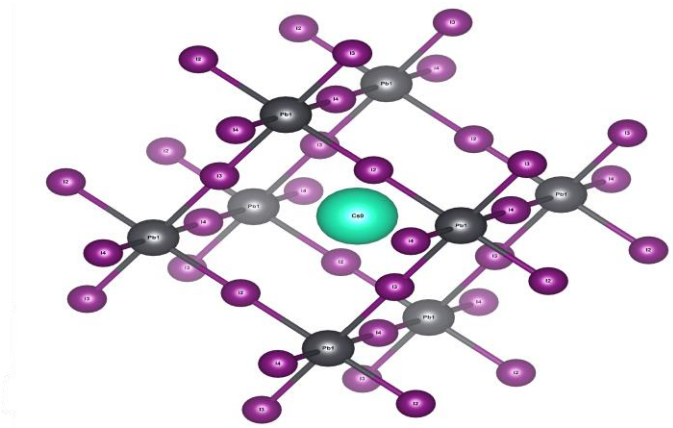

Figure 5. 5 Crystal system for $CsPbI_3$ cubic structure (Jain et al., 2013).

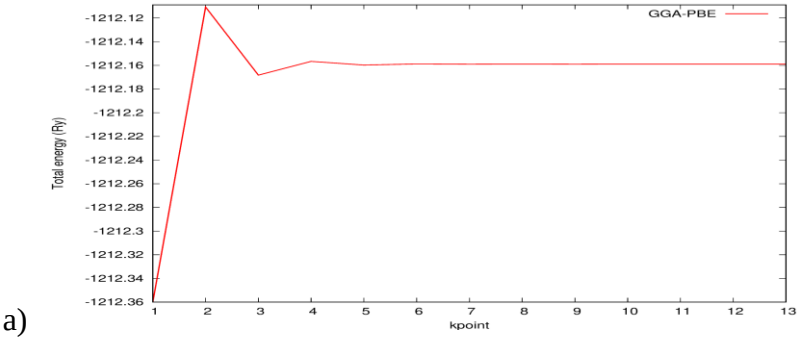

a)

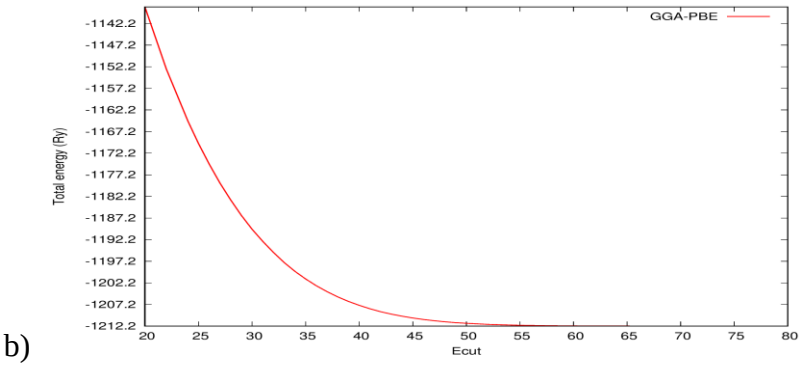

b)

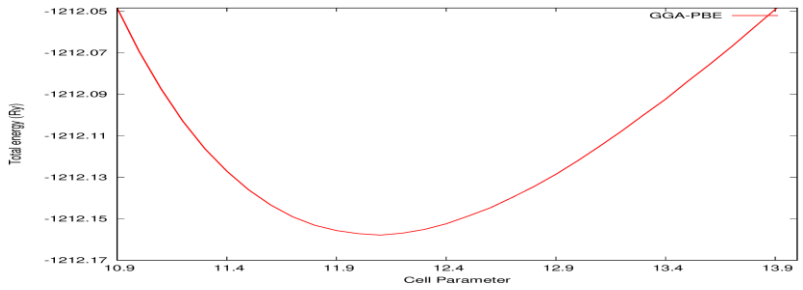

c)

Figure 5.6 Convergence graphs for cubic $CsPbI_3$ based on GGA-PBE functional with norm-conserving pseudopotentials; a) k-points, b) cut-off energy and c) cell parameter convergence.

Begining with GGA-PBE, five k-points and ecut of 60 Ry were used. The curve obtained from plotting energy values against cell parameter is shown in figure 5.6 (c). For GGA-PBEsol, the k-point, ecut and cell parameter versus energy graphs are shown in figure 5.7.

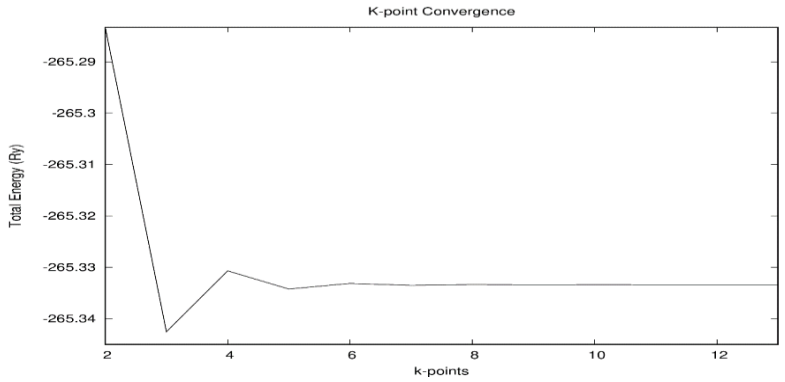

a)

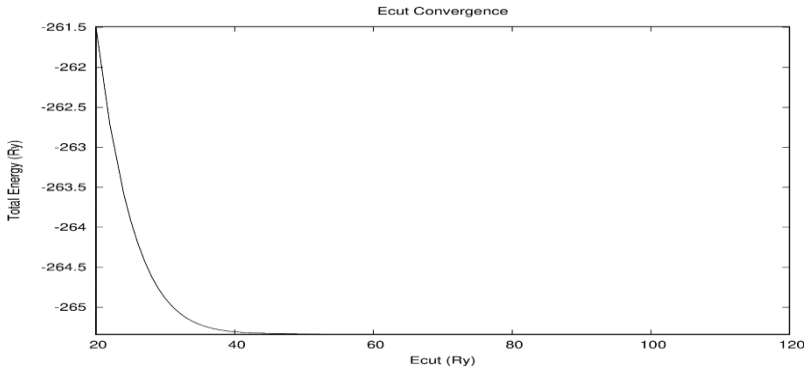

b)

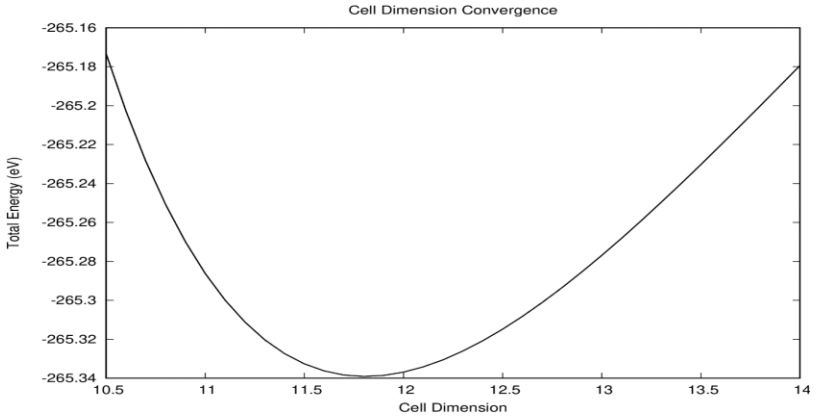

c)

Figure 5.7 Convergence graphs for cubic $CsPbI_3$ based on GGA-PBEsol functional with norm-conserving pseudopotentials; a) k-points, b) cut-off energy and c) cell parameter convergence.

Fitting the energy against cell parameters in the equation of state, the following results were obtained: a_0 = 11.8008 a.u., k_0 = 159 kbar, emin = -265.33766 and V_0 = 1643.37 $(a.u.)^3$ (Parameters a_0, k_0, and V_0 are equilibrium lattice parameter, bulk modulus, and equilibrium cell volume respectively).

5.2 Elastic Properties

5.2.1 Elastic Properties for Cubic $CsPbI_3$

5.2.1.1 Elastic Constants Calculated using thermo_pw code for Cubic $CsPbI_3$ using GGA approximation method.

The following elastic constants for cubic $CsPbI_3$ were calculated based on GGA-PBE and GGA-PBEsol approximation, Bulk Modulus, Sheer Modulus, Young's Modulus and Poisson's Ratio. The bulk modulus calculated depict a flexible material.

Table 5.1 Elastic Constants for cubic $CsPbI_3$ calculated based on GGA-PBE and GGA-PBEsol Functionals.

Elastic Constant		**Approximation**			**Experimental Results**
		Voigt	**Reuss**	**Voigt-Reuss-Hill Average**	
Bulk Modulus (B) (kbar)	PBE	147.87766	147.8776	147.8776	146
	PBEsol	149.38576	149.38576	149.38576	
Young Modulus (E) (kbar)	PBE	205.81754	137.61921	171.71837	-
	PBEsol	220.36176	136.39253	178.37715	
Shear Modulus (G) (kbar)	PBE	81.1563	51.16354	66.15992	-
	PBEsol	87.85325	50.59710	69.22518	
Poisson Ratio (n)	PBE	0.26803	0.34490	0.29775	-
	PBEsol	0.25415	0.34783	0.28838	

5.2.1.2 Birch-Murnaghan Equation of state

Energy and pressure-volume values were fitted into the equation of state yielding the equilibrium volume of 1762.3130 $(a.u)^3$ and 1693.6131 $(a.u.)^3$ for GGA-PBE and GGA-PBEsol respectively for the cubic structure. Equation of state calculated based on GGA-PBE and GGA-PBEsol approximations shows the corresponding relationship between energy/ pressure and volume of the material as shown in figure 5.8.

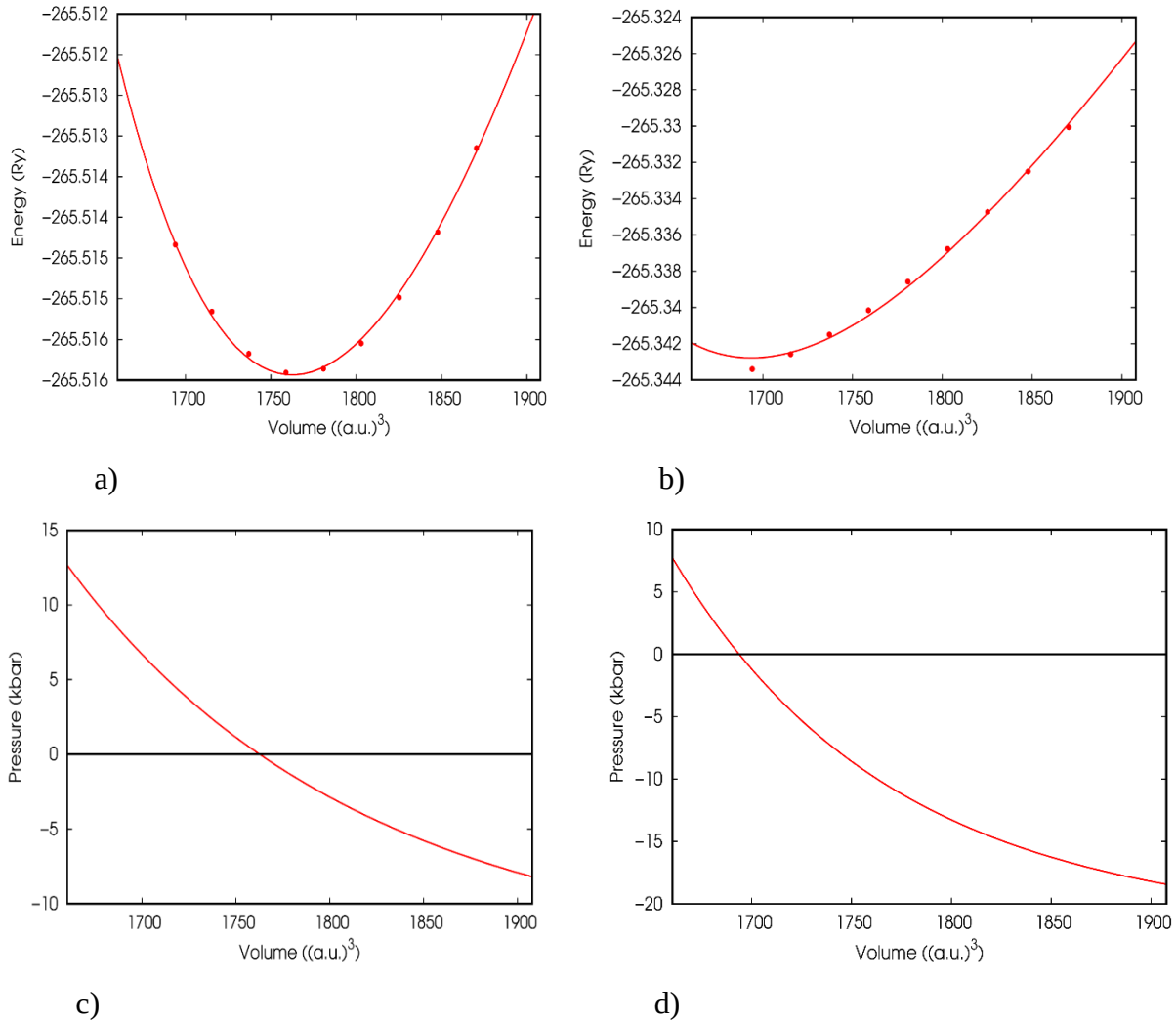

Figure 5.8 Energy and pressure values fitted into the equation of state calculated based on: a) and c); GGA-PBE, b) and d); GGA-PBEsol functional for the cubic structure.

5.2.1.3 Predictions based on Debye Model.

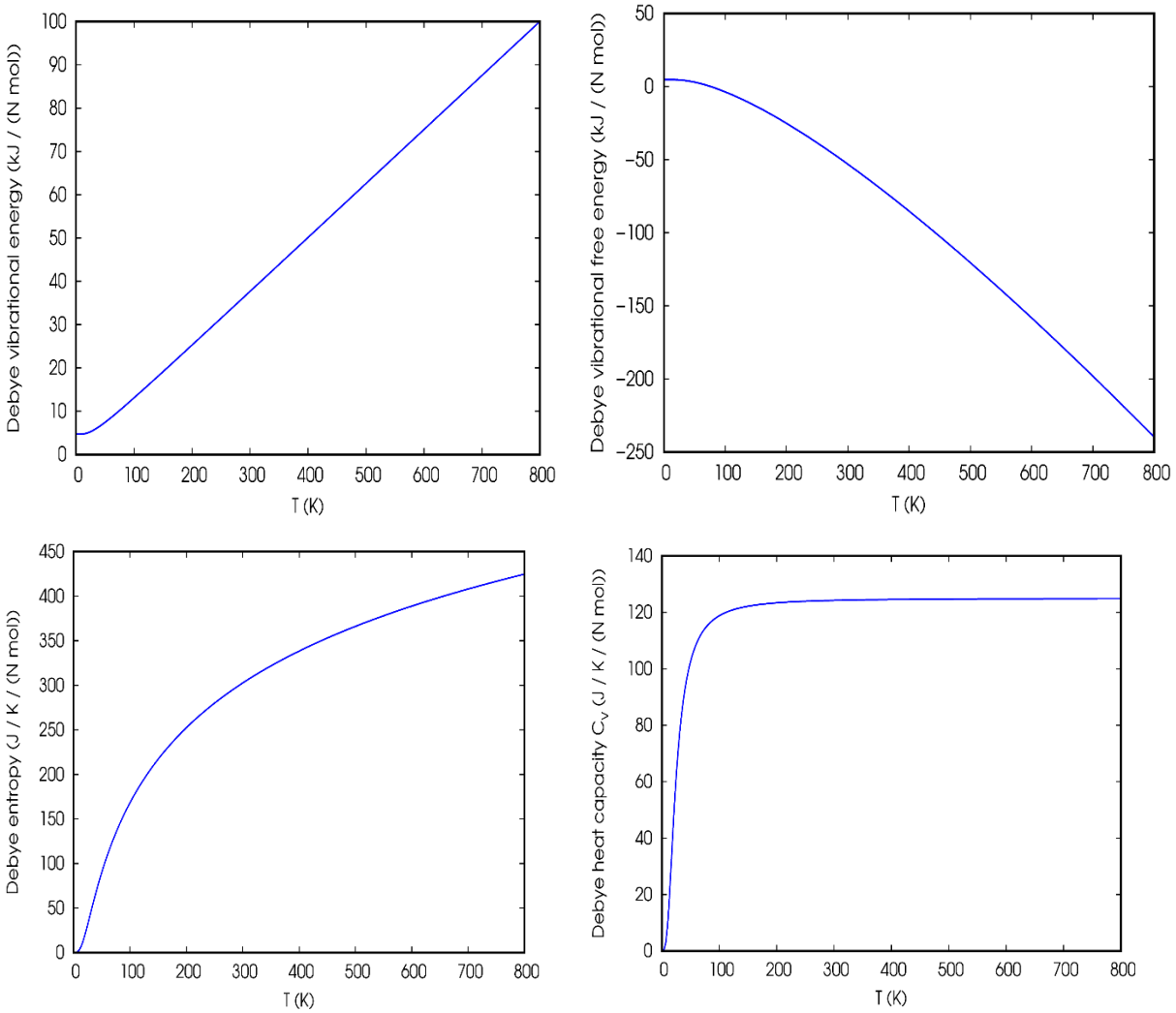

Figure 5.9 Predictions of Vibrational Energy, Vibrational Free Energy, Entropy and Heat Capacity of Cubic $CsPbI_3$ using GGA approximation method for the cubic structure.

5.2.2 Elastic Properties for Orthorhombic $CsPbI_3$

5.2.2.1 Elastic Constants Calculated using thermo_pw code for Orthorhombic $CsPbI_3$ using GGA-PBEsol approximation method.

The following elastic constants in table 5.2 for orthorhombic $CsPbI_3$ were calculated based on GGA-PBEsol approximation method.

Table 5.2 Elastic Constants for orthorhombic $CsPbI_3$ calculated based on GGA-PBEsol Functional.

Elastic Constant		Approximation		
		Voigt	**Reuss**	**Voigt-Reuss-Hill Average**
Bulk Modulus (B) (kbar)	PBEsol	69.57221	69.28118	69.42670
Young Modulus (E) (kbar)	PBEsol	130.48223	110.06545	120.27384
Shear Modulus (G) (kbar)	PBEsol	54.94369	44.55296	49.74833
Poisson Ratio (n)	PBEsol	0.18742	0.23522	0.20882

5.2.2.2 Birch-Murnaghan Equation of state

The equilibrium volume for Orthorhombic $CsPbI_3$ obtained by fitting pressure-volume values into the equation of state yielded the equilibrium volume of 6501.2127 $(a.u.)^3$ for GGA-PBEsol. The graphs drown from Pressure/Energy-volume values are as shown in figure 5.10.

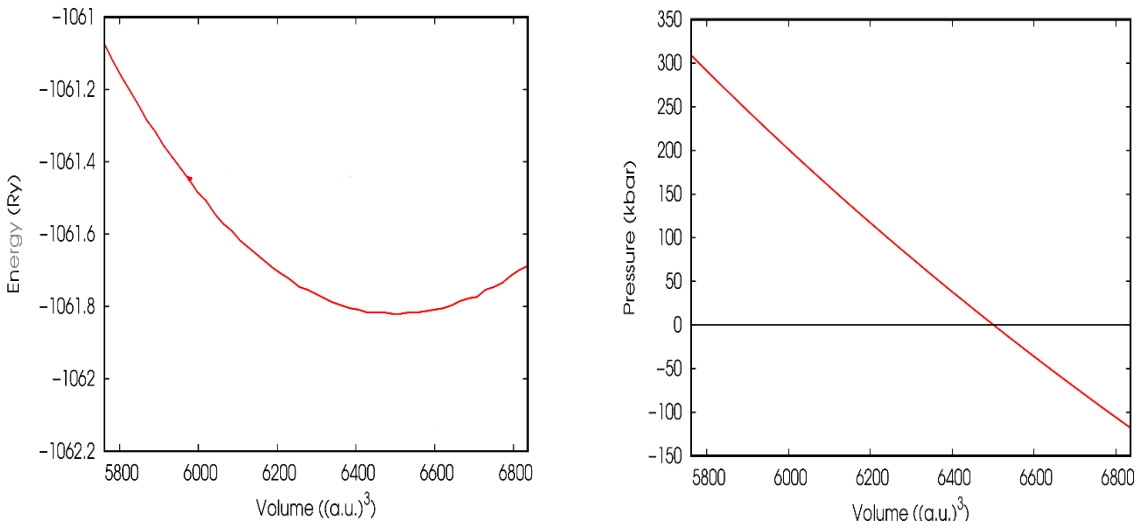

a) b)

Figure 5.10 Energy and pressure values fitted into the equation of state calculated based on GGA-PBEsol functional for the orthorhombic structure.

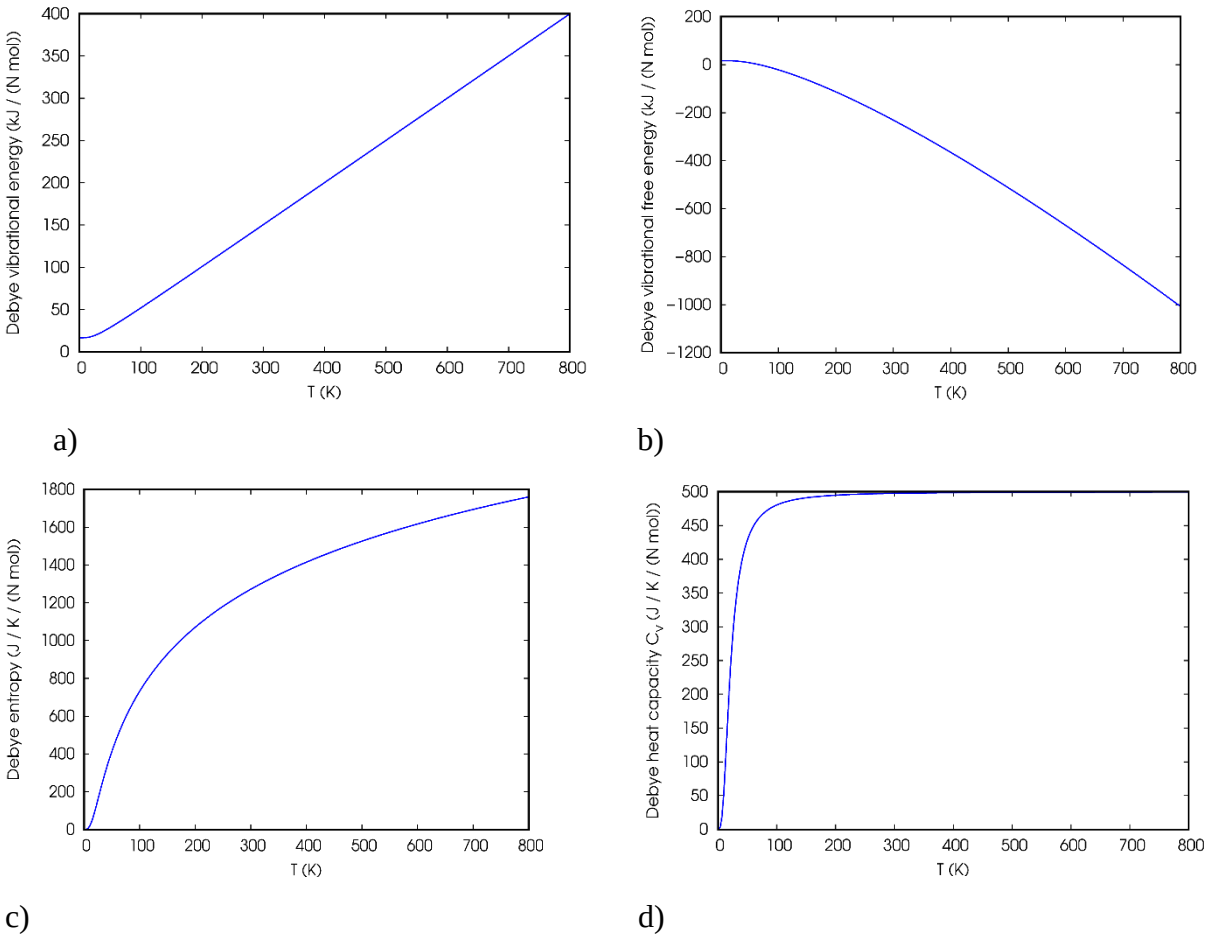

Figure 5.11 Predictions of Vibrational Energy, Vibrational Free Energy, Entropy and Heat Capacity of Orthorhombic $CsPbI_3$ using GGA-PBEsol approximation method for the orthorhombic structure.

5.3 Electronic Properties

5.3.1 Band Structure for Orthorhombic $CsPbI_3$ with PBE functional

The dependence of electronic energies on k-vector was determined along the directions of symmetry in the Brillouin zones (with paw pseudopotential) and expressed graphically as shown in fig 5.12.

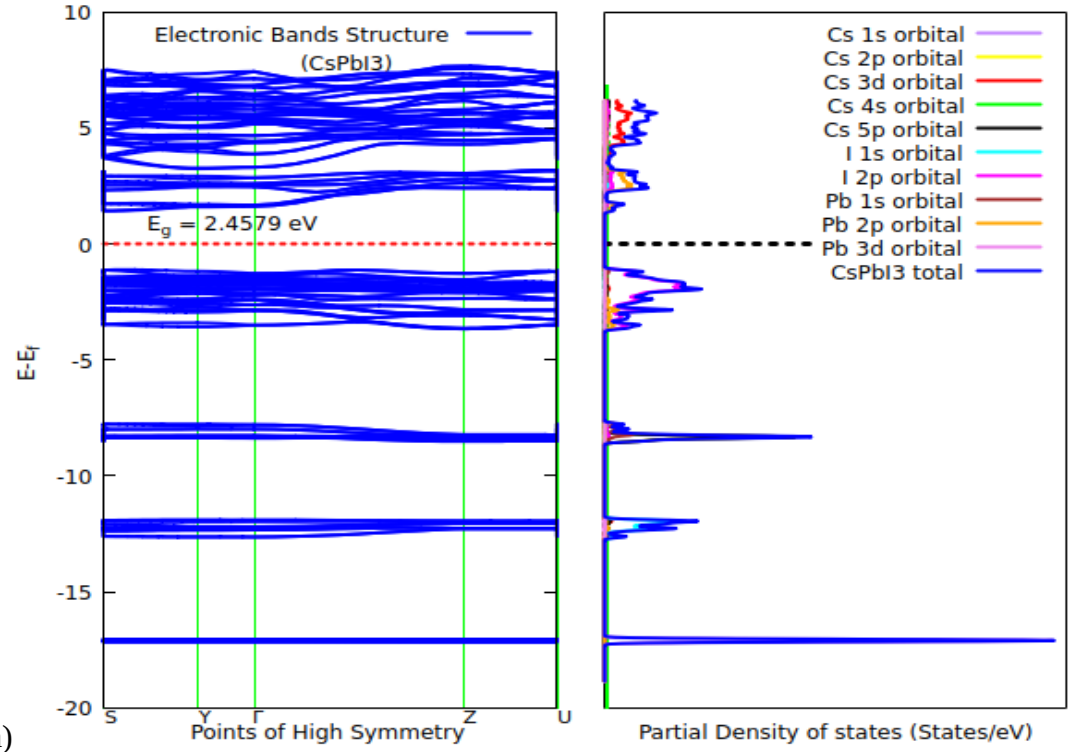

a)

Figure 5.12 Graphs of a) Bands and PDOS calculated based on GGA-PBE functional with PAW pseudopotentials.

This material, from the Pnma space group, has a direct band gap of 2.4579 eV as deduced from the energy difference at a selected point of high symmetry. This value of band gap is close to 2.58 eV reported by (Kaczkowski and Płowaś-Korus, 2021). However, because this is calculated at room temperature, it has little applicability owing to its proximity to the yellow non-perovskite phase. Treatment at higher temperature would, therefore, be necessary to shift it from the unsuitable, yellow non-perovskite δ-polymorph. A more stable black-phase would be achieved at higher temperatures. This would, however, yield an α-$CsPbI_3$, β- $CsPbI_3$ or γ-$CsPbI_3$ polymorphs(Kaczkowski and Płowaś-Korus, 2021). The conduction band is dominated by Cs 3(d) and Pb 2(p) states. Other minor contributors are Cs 4(s), Cs 5(p), I 2(P), and Pb 3(d) states.

The band structure generated for orthorhombic $CsPbI_3$ when norm conserving pseudopotentials were used is shown in figure 5.13. The plot shows a direct band gap of 2.321346 eV with the conduction band being dominated by Pb 5(p) and I 3(p) states. The minor contributor is I 2(s) state.

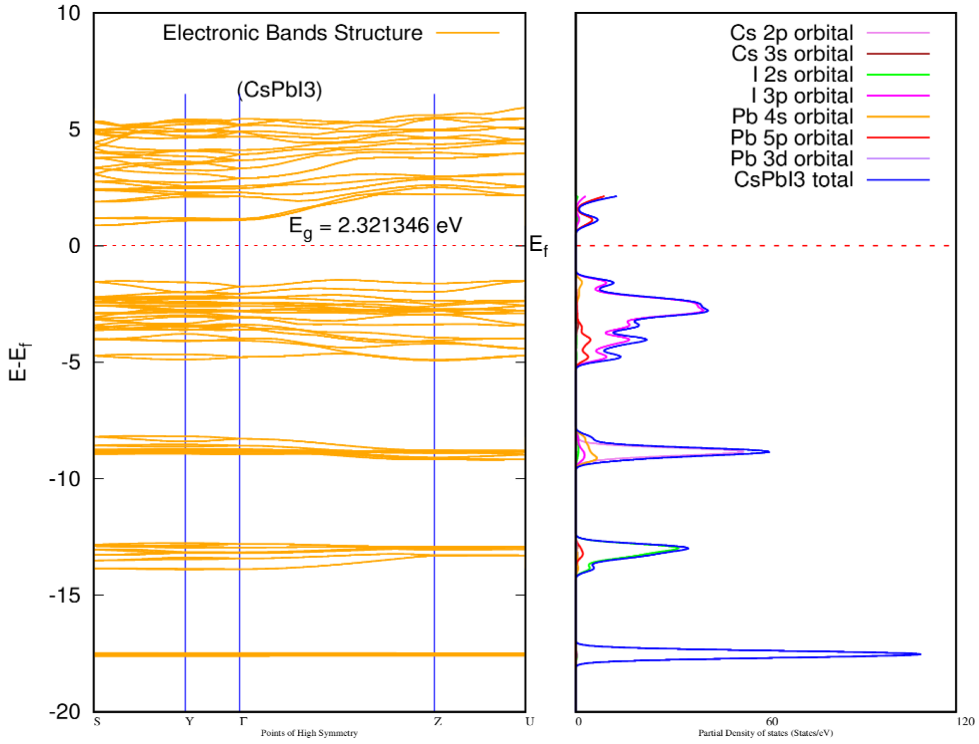

Figure 5.13 Graphs of a) Bands and PDOS for orthorhombic $CsPbI_3$ calculated based on GGA-PBE functional with norm-conserving pseudopotentials.

5.3.2 Band Structure for Orthorhombic $CsPbI_3$ calculated based on GGA-PBEsol functional.

The band structure for orthorhombic $CsPbI_3$ generated based on GGA-PBEsol functional with norm conserving pseudopotentials yielded a direct band gap of 2.39372 eV as shown in figure 5.14. The major contributing states to the conduction band are Pb 3(p) and I 2(p) states, while the minority contributing state is I 1(s) state.

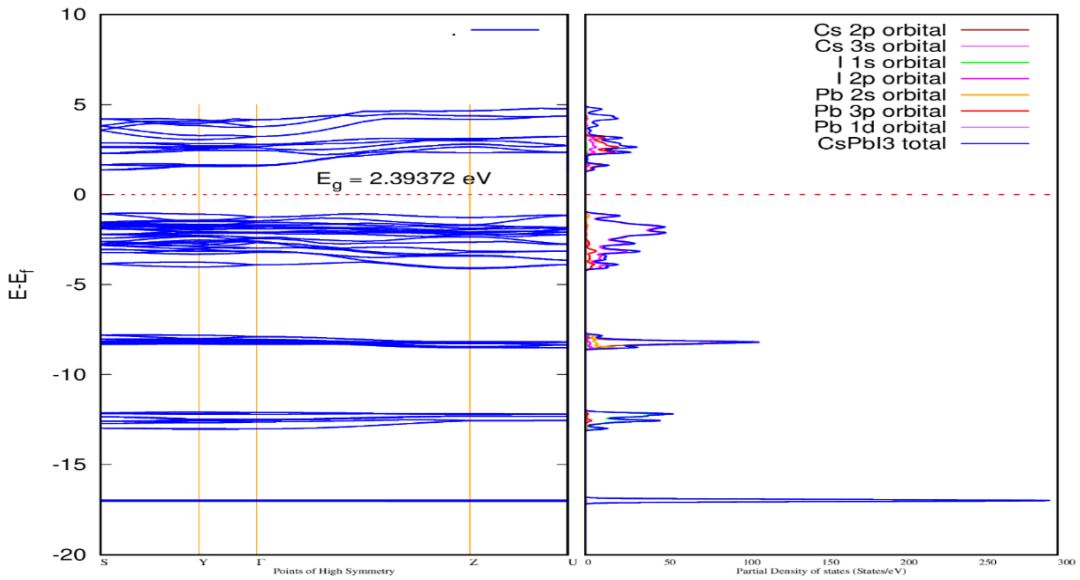

Figure 5.14 Graphs of Bands and PDOS for orthorhombic $CsPbI_3$ calculated based on GGA-PBEsol functional with norm-conserving pseudopotentials.

5.3.3 Band Structure for Cubic $CsPbI_3$ calculated based on GGA-PBE functional.

A cubic structure generated using GGA-PBE norm-conserving pseudopotentials has a direct band gap of 1.195219 eV. This bandgap is underestimated compared to the experimental value of 1.73 eV, in agreement with the findings of (Liu *et al*., 2020). However, this cubic phase has the smallest bandgap. It is more symmetrical and is most suitable for photovoltaic applications. However, it is only stable above 300 ^{o}C, a temperature below which it changes to a non-perovskite, yellow δ-phase, unsuitable polymorph. The states that dominate the conduction band are Cs 3(s), I 2s, I 3(p), and Pb 5(p). A minor contribution is made by I 2(s) state.

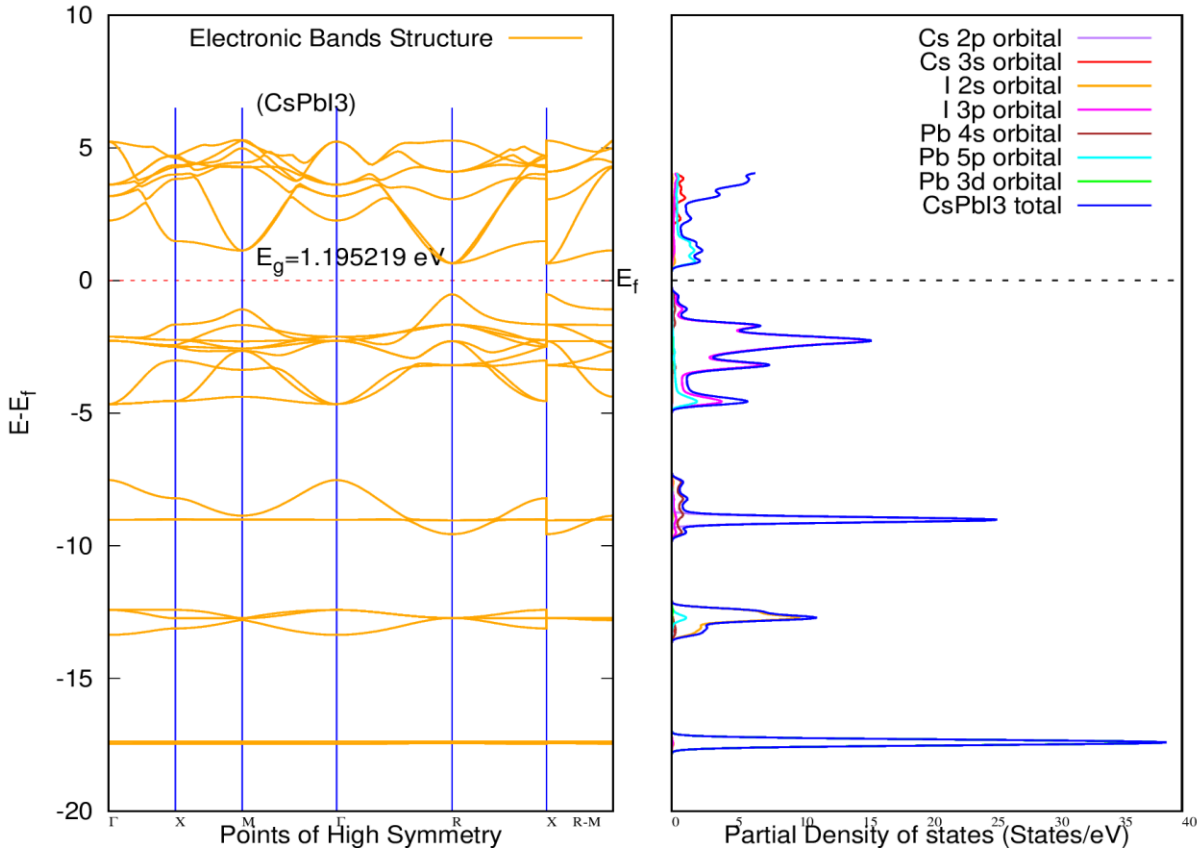

Figure 5.15 Graphs of Bands and PDOS for cubic $CsPbI_3$ calculated based on GGA-PBE functional with norm-conserving pseudopotentials.

5.3.4 Band Structure for Cubic $CsPbI_3$ calculated based on GGA-PBEsol functional.

The band structure shown in fig 5.16 was generated using GGA-PBEsol pseudopotentials, giving a band gap of 1.169895 eV. This band gap is also suitable for photovoltaic applications. However, it is also underestimated like the one obtained from the band diagram in figure 5.15. The orbitals that dominate the conduction band are Cs 3(s), Pb 3(p), I 1(s) and I 2(p).

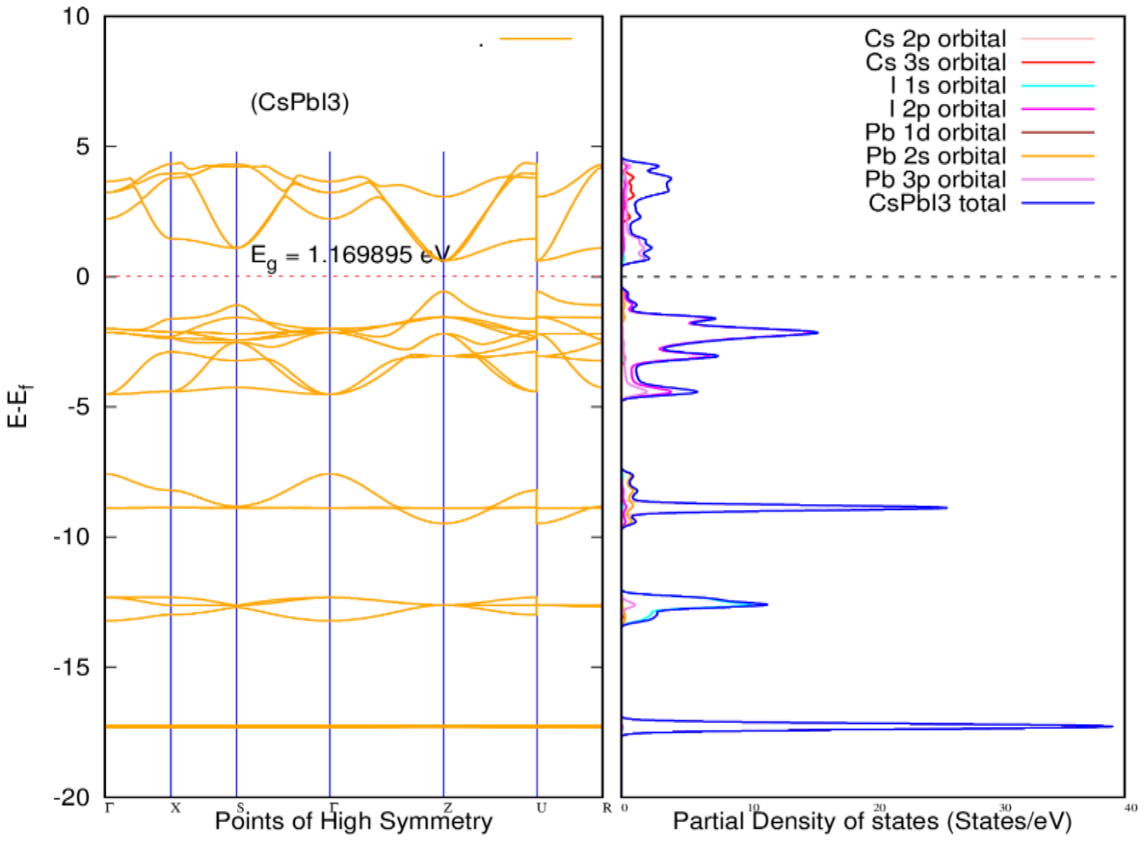

Figure 5.16 Graphs of Bands and PDOS for cubic $CsPbI_3$ calculated based on GGA-PBEsol functional with norm-conserving pseudopotentials.

5.4 Optical Properties

5.4.1 Optical Properties for Orthorhombic $CsPbI_3$ with GGA-PBE

From the graphs in 5.17 (c) and (d), it is possible to identify some degree of anisotropy in the dielectric tensor arising from the deference in the energy peaks. These peaks are associated with inter-band transitions between the valence and conduction bands. As shown in figure 5.17 (a)-(h), for the resolved reflectance in the real region, reflectivity increases gradually with energy of incident radiation for 0 eV and peaks at between 3 and 3.5 eV. However, the highest reflectance peak in the real region is observed at about 4 eV in the x-direction and the lowest in the z-direction. The lowest peak lies at about 4 eV which is an ultraviolet region. The highest peak is in the x-direction and lowest in the y-direction. In the imaginary region, the highest resolved reflectance lies between 0 eV and 2 eV and the lowest lies between 3.5 eV and 4 eV. The highest refractive index peak in the x-direction lies at about 3 eV and lowest at 4 eV in the

x-direction. For the imaginary part of refractive index, the highest peak lies at about 4.5 eV in the x-direction, while lowest between; 0 eV and 2 eV in the y and z-directions and between 3.5eV and 4 eV in the x-direction. The highest imaginary and real refractive index peaks for the resolved case are both highest at about 3.2 eV, with the imaginary case being lowest between 0 and 2 eV. The electron loss rises sharply at 10eV.

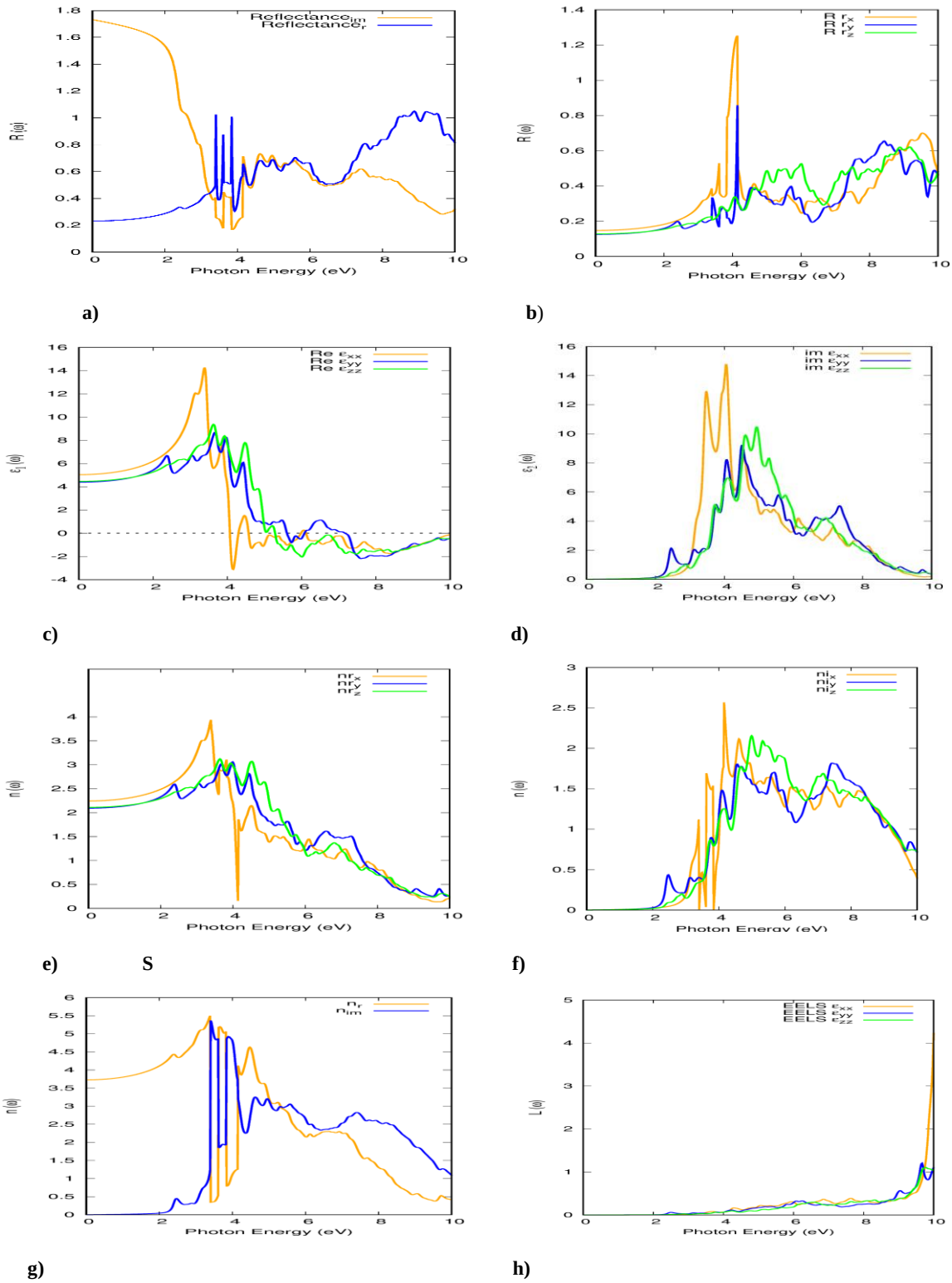

Figure 5.17 Graphs of photon energy against a) reflectance for imaginary and real parts, b) reflectance in the x, y and z polarizations, c) real part of dielectric tensor in the x, y and z polarizations, d) imaginary part of dielectric tensor in the x, y and z polarizations, e) real part of refractive index in the x, y and z polarizations, f) imaginary part of refractive index in the x, y and z polarizations, g) resultant real and imaginary parts of refractive index and h) electron loss in the x, y and z polarizations.

5.4.2 Optical Properties for Cubic System of $CsPbI_3$ with GGA-PBE

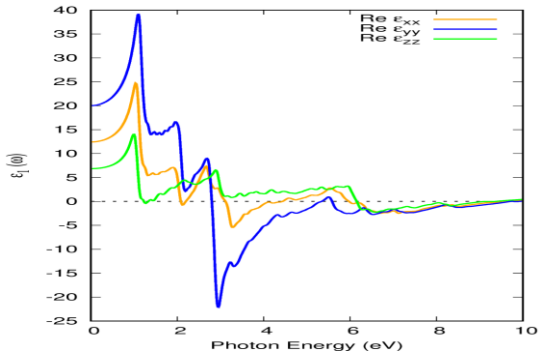

a)

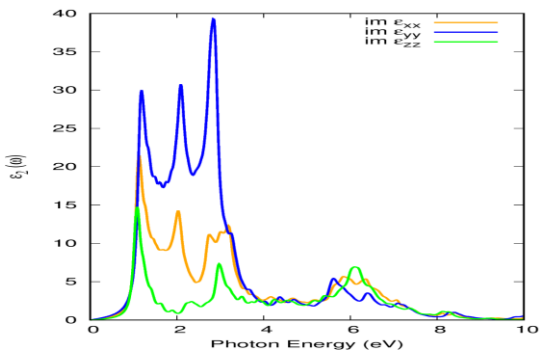

b)

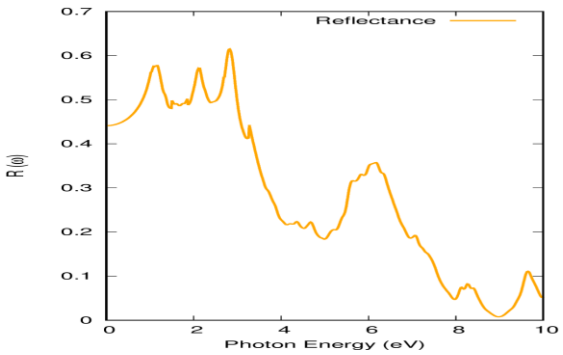

c)

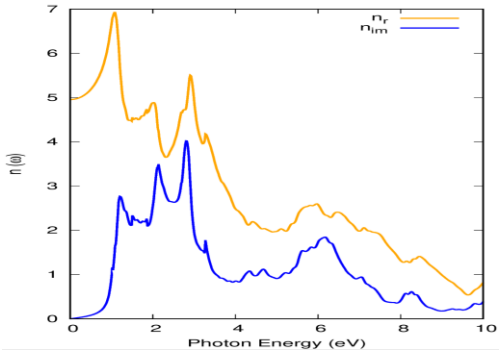

d)

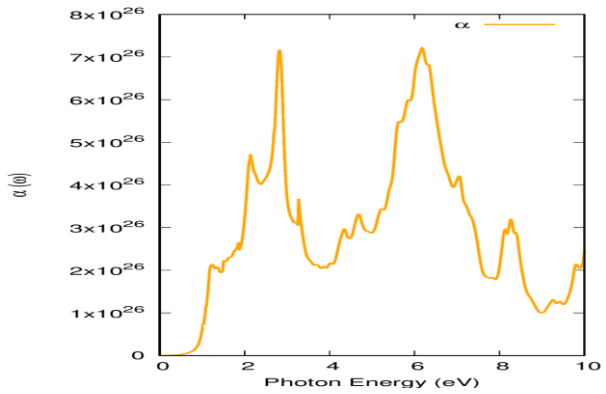

f)

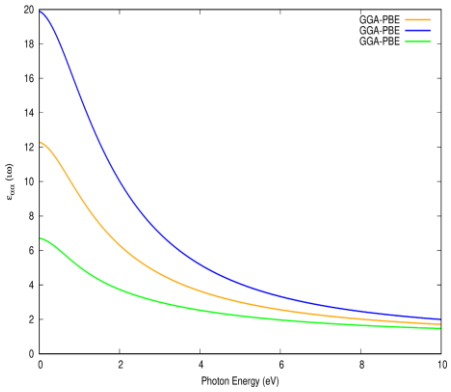

e)

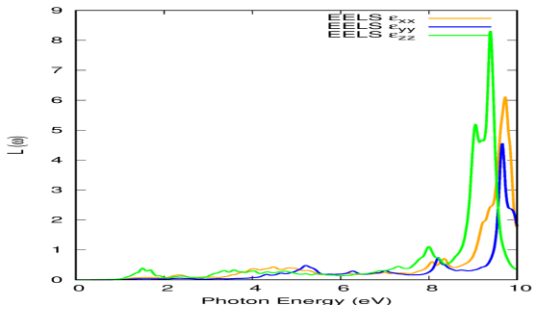

g)

Figure 5.18 Graphs of; a) real part of dielectric tensor in x, y and z polarizations b) imaginary part of dielectric tensor in x, y and z polarizations, c) reflectance d) real and imaginary refractive indices, e) absorption coefficient and f) diagonal components of dielectric tensor derived from the imaginary axe of frequency and g) electron energy loss spectrum as a function of photon energy.

In the case of the cubic system, the calculations were carried out based on GGA-PBE functional. The highest peaks of reflectance were observed to lie between 1.0 and 3.0 eV, and the lowest at 9 eV. The real component of refractive index had the highest peak at about 1 eV, while the imaginary component had its highest peak at about 3 eV. Absorptance of incident radiation increases sharply and peaks at about 2.5 eV, which is within the visible region, followed by a sharp drop and another peak at 6 eV out of the visible region as shown in fig 5.18 (e). Electron energy loss remains negligibly low and then rises sharply from about 8.5 eV as indicated in figure 5.18 (g). The degree of polarization of incident radiation is given in fig 5.18 (a), with the highest peaks being in the y-direction when the energy of incident radiation is at about 1 eV and 3 eV respectively. Fig 5.18 (b) indicates the loss factor (Energy absorbed/m^3), where the highest ability to absorb visible incident radiation being at 3 eV in the y-direction.

5.4.3 Optical properties for Cubic System of $CsPbI_3$ with GGA-PBEsol

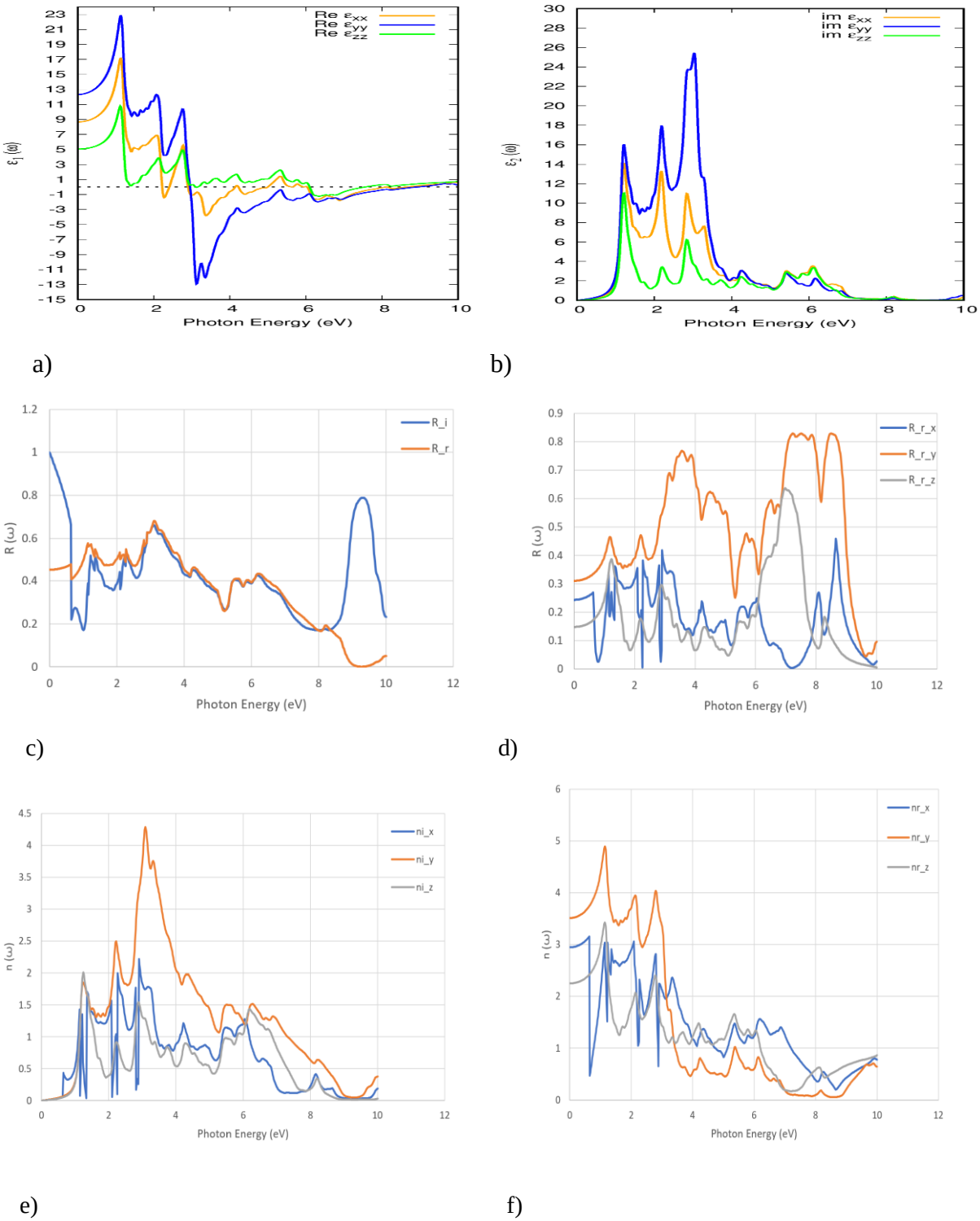

Figure 5.19 Graphs of photon energy against; a) real part of dielectric tensor b) imaginary part of dielectric tensor c) resolved real and imaginery parts of reflectance d) real part of reflectance in x, y and z directions e) real part of refractive index in x, y and z directions f) real part of refractive index in x, y and z.

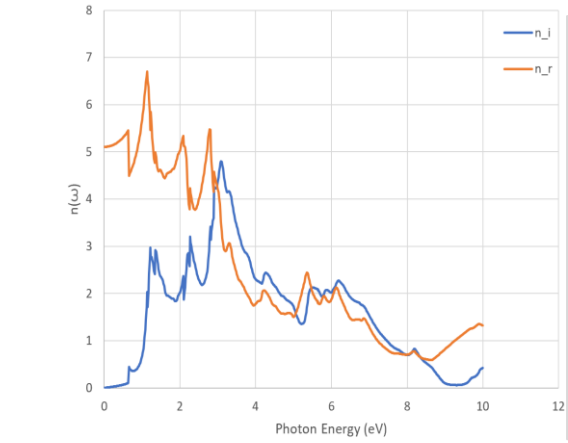

a)

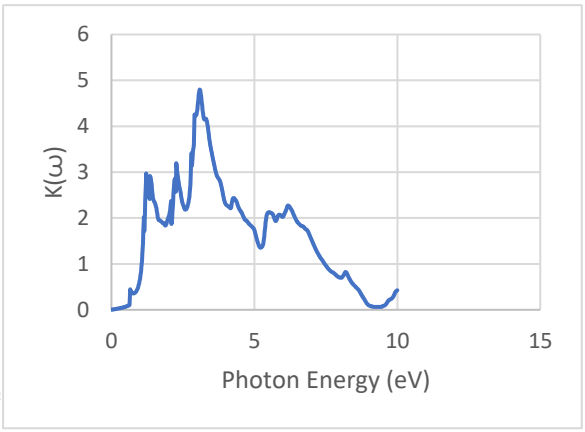

b)

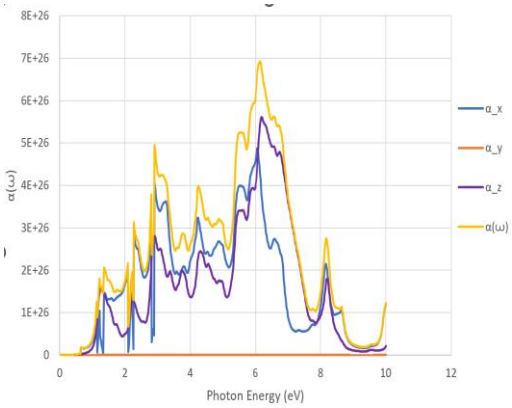

c)

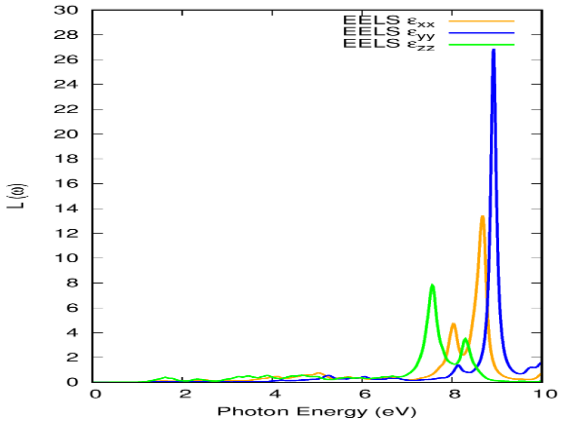

d)

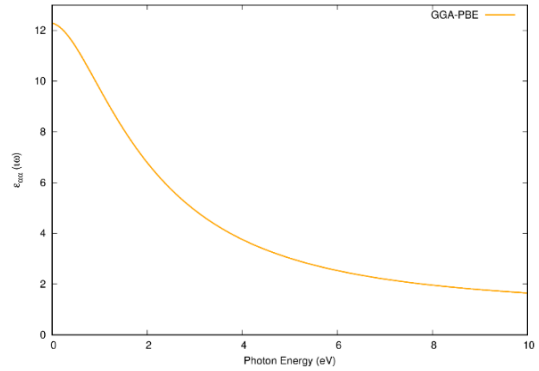

e)

Figure 5.20 Graphs of photon energy against; a) resolved real and imaginary parts of refractive index b) extinction coefficient c) absorption coefficient d) electron loss coefficient e) diagonal component of dielectric tensor.

The calculations carried out based on PBEsol at constant pressure gave spectral graphs with the highest peaks for real part of dielectric constant at about 1 eV and 3 eV in the y-direction (Fig 5.19 a). This real part gives the intra-band transitions and has two peaks which are because

of absorption by free electrons (i.e., bulk plasmons excitations). No wave goes through this medium between 1.7 eV and 8 eV in the x and y-directions. Absorptivity is found to be strong where real component of the dielectric constant ($\mathcal{E}_1$) has a high peak, while optical conductivity is low. From the real part of dielectric constant, static refractive index can be obtained from equation 5.1. Table 5.3 gives a summary of refractive indices for different light polarizations.

$$n(0) = \sqrt{[Re\ \mathcal{E}(0)]} \quad \ldots\ldots (5.1)$$

Table 5.3 Static refractive indices for $CsPbI_3$ as calculated from real part of dielectric constant.

	Static Refractive Index			**Maximum imaginary Refractive Index**			**Reference**
Polarized light direction	x	y	z	x	y	z	
GGA-PBE (Cubic)	3.536	4.472	2.646	Effective n = 4.0			
GGA-PBEsol (Cubic)	2.915	3.493	2.236	2.25	4.25	2.0	
GGA-PBE (Orthorhombic)	2.236	2.121	2.121	2.65	1.80	2.18	
Experimental	2.46						(Singh *et al.*, 2019)

For the imaginary part, which gives the inter-band transitions, the highest peak lies at 3 eV (in agreement with experimental results) as shown in figure 5.20. This highest peak is the point of inter-band transition from occupied valence band to unoccupied conduction band. The other two shorter peaks show the transition to the conduction band from semi-core states. There is negligible/ slow increment in the imaginary part between 0 and 1 eV, which explains the low absorptivity in this region. This region is the optical gap which the first direct optical transition. Three major peaks are observed, which agrees with experimental results, at 1, 2 and 3 eV. Reflectivity for both imaginary and real parts are at highest peak at about 3 eV and remains similar while dropping gradually between 2 eV and 8 eV. It is notable from fig 5.19 (d) that

the highest reflectivity in the real part is in the y-direction. Greatest refractive indices for the imaginary and real components are in the y-direction when the energies of incident radiation are about 3 eV and 1 eV respectively. Highest electron loss coefficient lies about the same energy of 3 eV, with a shorter peak at about 1 eV. Absorption coefficient is minimum in the y-direction and maximum ion the z and x directions in decreasing order at 6 eV and 3 eV respectively. Electron loss coefficient remains negligible up to 7 eV and peaks. In agreement with experimental results, the extinction coefficient peaks when the absorption coefficient is maximum withing the visible spectrum of 3 eV, indicating that it is a measure of optical absorptivity of a material as shown in figure 5.20 (b) and (c).

5.5 Lattice Vibrations

5.5.1 Phonon spectrum of cubic $CsPbI_3$ for GGA PBE

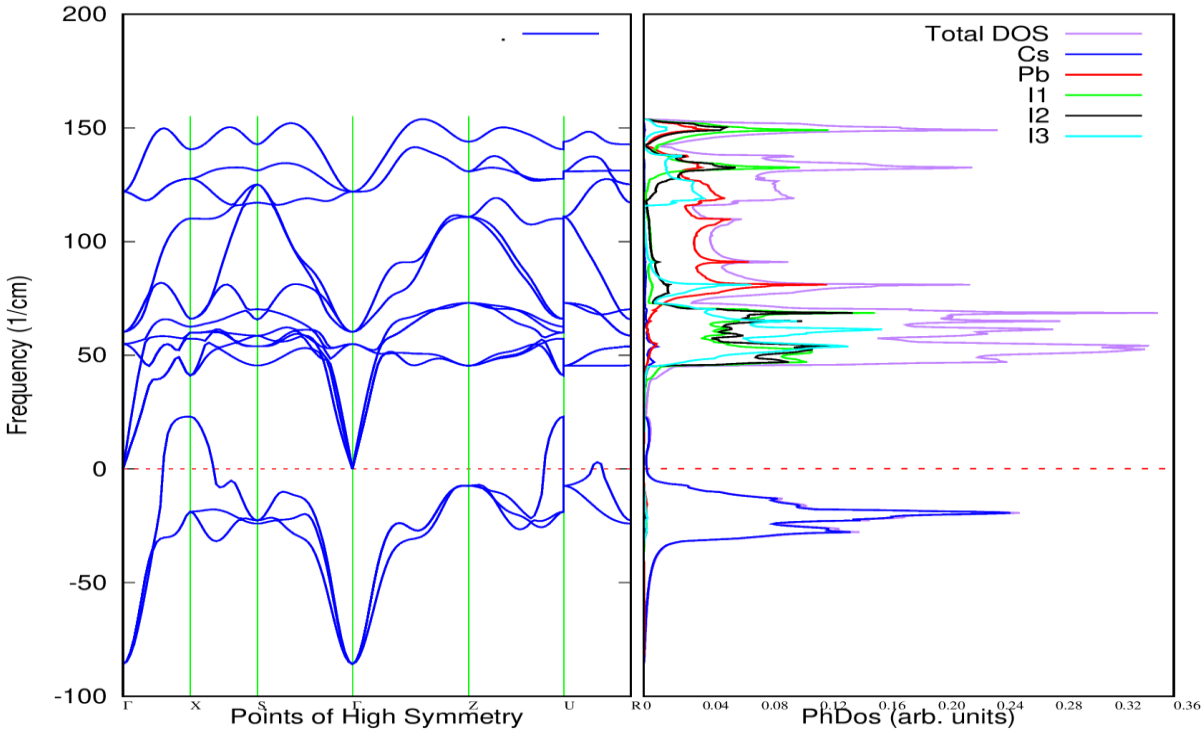

Figure 5.21 Curves of phonon spectrum for cubic $CsPbI_3$ with GGA-PBE functional.

The phonon dispersion relation was calculated based on 4x4x4 cubic mesh of q-points through diagonalization of dynamical matrix as implemented in the phonon code. Along with the phonon bands, phonon DOS was also calculated for the cubic structure. These were performed at low temperature while holding pressure/ volume constant, depicting modes with imaginary frequencies (soft modes). This, given the low symmetry observed, is a sign of dynamical instability depicted by the low-lying optical modes. This agrees with earlier finding that this material decomposes further from the cubic phase at low temperatures (T = 0) yielding a less-symmetrical structure (Kaczkowski & Płowaś-Korus, 2021; Liu *et al.*, 2020). The whole frequency range comprises four sections; negative frequency modes dominated by Cesium atoms, low frequency mode of about 50 cm^{-1} dominated by Iodine atoms and middle and higher frequency modes dominated by lead and iodine atoms. No vibrational modes were registered between 0 and 40 cm^{-1}.

5.5.2 Phonon spectrum of cubic $CsPbI_3$ for GGA PBEsol

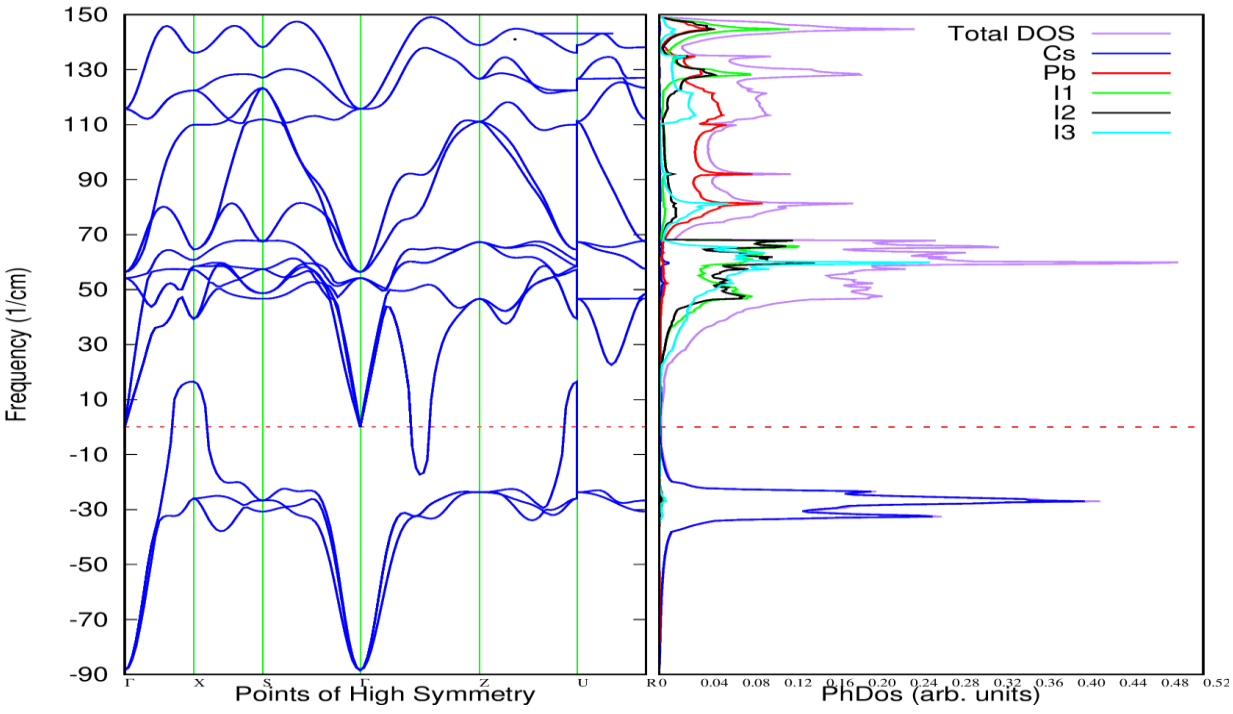

Figure 5.22 Curves of phonon dispersion and projected phonon density of state for cubic $CsPbI_3$ calculated based on GGA-PBEsol functional (accuracy 10^{-12})

When phonon calculation is based on GGA-PBEsol method, the dynamical instability as depicted in optical and acoustic modes in the GGA-PBE case persists, giving imaginary frequencies at the lower optical mode with a peak at -30cm^{-1} confirming the findings by (Kaczkowski and Płowaś-Korus, 2021) . The highest peak has a positive frequency with a peak at 50 cm^{-1} as shown in figure 5.22. No vibrational modes are registered between -10 cm^{-1} and 10 cm^{-1}. The highest frequency mode lies at about 145 cm^{-1}. The soft modes depict some magnitude of low symmetry in the material.

CHAPTER SIX: CONCLUSIONS AND RECOMMENDATIONS

6.1 Conclusion

DFT calculations have been carried out based on first principles to study electronic, optical, elastic and phonon properties of $CsPbI_3$ perovskite at constant pressure for; orthorhombic $CsPbI_3$ using GGA-PBE PAW pseudopotentials, Cubic $CsPbI_3$ using GGA-PBE and GGA-PBEsol approximation approach with norm conserving pseudopotentials. Both structures have been found to have direct bandgaps, in agreement with experimental results.

The calculated band gaps for both cubic and orthorhombic structures ranging from (1.169895-2.39372 eV) are averagely within the optimal range for incident visible and edge of ultraviolet light absorption for solar cell device applications. This makes these materials suitable for photovoltaic applications. However, the presence of soft modes shows that these material structures have slight dynamical instability at low temperatures. The instability was found to be persistent across all Brillouin zones.

The calculated refractive indices range between 1.5 eV and 3.5 eV, which is the visible range, comparable to the experimental value of 2.46. The highest optical absorption index was recorded within the visible region and narrowly at the beginning of ultraviolet region, making this material suitable for optoelectronic applications.

The phonon dispersion curves expose low symmetry and instability at low temperatures within the lower optical modes (soft modes), albeit with varied intensities across all the Brillouin zones. This small structural instability at low temperatures in α-$CsPbI_3$ phase explains the effect of phase transitions at different temperatures. Elastic calculations depict flexibility of the cubic $CsPbI_3$ structure.

6.2 Recommendations

Further calculations at higher pressure and temperature would be necessary to achieve stability at lower optical modes in all Brillion zones. To improve stability, cut-off energy of the plane wave may need to be increased. It would also be necessary to try out LDA approximation approach to establish higher stability while putting into account effects of pressure and temperature.

REFERENCES

Al Alwash, L., Bakhshayeshi, A., and Motie, I. (2021). First-principles calculations of electronic and optical properties of CuTaS3 semiconductor. In *Optical and Quantum Electronics* (Vol. **53**, Issue 8). https://doi.org/10.1007/s11082-021-03050-3

Alborznia, H., Amirian, S., & Nazirzadeh, M. (2022). Buckling variation effects on optical and electronic properties of GeP2S nanostructure: a first-principles calculation. *Optical and Quantum Electronics*, ***54***(10). https://doi.org/10.1007/s11082-022-04055-2

Albrecht, S., & Rech, B. (2017). Perovskite solar cells: On top of commercial photovoltaics. *Nature Energy*, ***2***(1). https://doi.org/10.1038/nenergy.2016.196

Al-Lehyani, I. H. (2021). A first-principle study of the stability and electronic properties of halide inorganic double perovskite Cs2PbX6 (X = Cl,I) for solar cell application. *Arabian Journal of Chemistry*, ***14***(2), 102920. https://doi.org/10.1016/j.arabjc.2020.102920

Barkhouse, D. A. R., Gunawan, O., Gokmen, T., Todorov, T. K., & Mitzi, D. B. (2015). Yield predictions for photovoltaic power plants:empirical validation,recent advances and remaining uncertainties. *Progress in Photovoltaics: Research and Applications*, ***20***(1), 6–11. https://doi.org/10.1002/pip

Barron, A. R. (2015). Cost reduction in the solar industry. *Materials Today*, ***18***(1), 2–3. https://doi.org/10.1016/j.mattod.2014.10.022

Belyakov, V. A., Burdov, V. A., Lockwood, R., & Meldrum, A. (2008). Silicon nanocrystals: Fundamental theory and implications for stimulated emission. In *Advances in Optical Technologies*. https://doi.org/10.1155/2008/279502

Billah, M., Hoose, T., Onanuga, T., Lindenmann, N., Dietrich, P., Wingert, T., Goedecke, M., Hofmann, A., Troppenz, U., Moehrle, M., Sigmund, A., Freude, W., & Koos, C. (2015). Multi-chip integration of lasers and silicon photonics by photonic wire bonding. *CLEO: Science and Innovations, CLEO-SI 2015*, 2267. https://doi.org/10.1364/CLEO_SI.2015.STu2F.2

Capelle, K. (2006). A bird's-eye view of density-functional theory. In *Brazilian Journal of Physics* (Vol. **36**, Issue 4 A). https://doi.org/10.1590/s0103-97332006000700035

Chen, J., Xu, Z., & Chen, Y. (2020). Introduction of density functional theory. In *Electronic Structure and Surfaces of Sulfide Minerals* (pp. 1–12). Elsevier. https://doi.org/10.1016/b978-0-12-817974-1.00001-6

Eperon, G. E., Paternò, G. M., Sutton, R. J., Zampetti, A., Haghighirad, A. A., Cacialli, F., & Snaith, H. J. (2015). Inorganic caesium lead iodide perovskite solar cells. *Journal of Materials Chemistry A*, *3*(39), 19688–19695. https://doi.org/10.1039/c5ta06398a

Gibson, A. E. (2019). Front Matter. In *Front Matter* (pp. P001–P004). https://doi.org/10.1039/9781788013512-fp001

Goesten, M. G., & Hoffmann, R. (2018). Mirrors of Bonding in Metal Halide Perovskites. *Journal of the American Chemical Society*, ***140***(40), 12996–13010. https://doi.org/10.1021/jacs.8b08038

Gourji, F. H., & Velauthapillai, D. (2021). A review on Cs-based Pb-free double halide perovskites: From theoretical and experimental studies to doping and applications. In *Molecules* (Vol. **26**, Issue 7). MDPI AG. https://doi.org/10.3390/molecules26072010

Green, M. A., Ho-Baillie, A., & Snaith, H. J. (2014). The emergence of perovskite solar cells. In *Nature Photonics* (Vol. **8**, Issue 7, pp. 506–514). Nature Publishing Group. https://doi.org/10.1038/nphoton.2014.134

Haeger, T., Heiderhoff, R., & Riedl, T. (2020). Thermal properties of metal-halide perovskites. *Journal of Materials Chemistry C*, ***8***(41), 14289–14311. https://doi.org/10.1039/d0tc03754k

Hoffman, D. P., Leblebici, S. Y., Schwartzberg, A. M., & Mathies, R. A. (2015). Exciton Mobility in Organic Photovoltaic Heterojunctions from Femtosecond Stimulated Raman. In *Journal of Physical Chemistry Letters* (Vol. **6**, Issue 15). https://doi.org/10.1021/acs.jpclett.5b01436

Idrissi, S., Labrim, H., Bahmad, L., & Benyoussef, A. (2021). DFT and TDDFT studies of the new inorganic perovskite CsPbI3 for solar cell applications. *Chemical Physics Letters*, *766*(January), 138347. https://doi.org/10.1016/j.cplett.2021.138347

Jain, A., Ong, S. P., Hautier, G., Chen, W., Richards, W. D., Dacek, S., Cholia, S., Gunter, D., Skinner, D., Ceder, G., & Persson, K. A. (2013). Commentary: The materials project: A materials genome approach to accelerating materials innovation. *APL Materials*, ***1***(1). https://doi.org/10.1063/1.4812323

Kaczkowski, J., & Płowaś-Korus, I. (2021). The Vibrational and Thermodynamic Properties of CsPbI3Polymorphs: An Improved Description Based on the SCAN meta-GGA Functional. *Journal of Physical Chemistry Letters*, ***12***(28), 6613–6621. https://doi.org/10.1021/acs.jpclett.1c01798

Kang, Y., & Han, S. (2018). Intrinsic Carrier Mobility of Cesium Lead Halide Perovskites. *Physical Review Applied*, ***10***(4). https://doi.org/10.1103/PhysRevApplied.10.044013

Killam, A., Reblitz, T., Augusto, A., & Bowden, S. (2017). All silicon tandem solar cell. *2017 IEEE 44th Photovoltaic Specialist Conference, PVSC 2017*, 508–511. https://doi.org/10.1109/PVSC.2017.8366565

Lahourpour, F., Boochani, A., Parhizgar, S. S., & Elahi, S. M. (2019). Structural, electronic and optical properties of graphene-like nano-layers MoX2(X:S,Se,Te): DFT study. In *Journal of Theoretical and Applied Physics* (Vol. **13**, Issue 3, pp. 191–201). https://doi.org/10.1007/s40094-019-0333-4

Li, F., Zhou, S., Yuan, J., Qin, C., Yang, Y., Shi, J., Ling, X., Li, Y., & Ma, W. (2019). Perovskite Quantum Dot Solar Cells with 15.6% Efficiency and Improved Stability Enabled by an α-CsPbI3/FAPbI3 Bilayer Structure. *ACS Energy Letters*, ***4***(11), 2571–2578. https://doi.org/10.1021/acsenergylett.9b01920

Li, Z., Xu, B., Liang, D., & Pan, A. (2020). Polarization-Dependent Optical Properties and Optoelectronic Devices of 2D Materials. *Research*, ***2020***, 1–35. https://doi.org/10.34133/2020/5464258

Ling, X., Zhou, S., Yuan, J., Shi, J., Qian, Y., Larson, B. W., Zhao, Q., Qin, C., Li, F., Shi, G., Stewart, C., Hu, J., Zhang, X., Luther, J. M., Duhm, S., & Ma, W. (2019). 14.1% CsPbI3 Perovskite Quantum Dot Solar Cells via Cesium Cation Passivation. *Advanced Energy Materials*, ***9***(28). https://doi.org/10.1002/aenm.201900721

Liu, D., Zha, W., Guo, Y., & Sa, R. (2020). Insight into the improved phase stability of CsPbI3 from First-Principles Calculations. *ACS Omega*, ***5***(1), 893–896. https://doi.org/10.1021/acsomega.9b03838

Maqbool, M., Rehman, G., Ali, L., Shafiq, M., Iqbal, R., Ahmad, R., Khan, T., Jalali-Asadabadi, S., Maqbool, M., & Ahmad, I. (2017). Structural, electronic and optical properties of CsPbX3(X=Cl,

Br, I) for energy storage and hybrid solar cell applications. *Journal of Alloys and Compounds*, ***705***, 828–839. https://doi.org/10.1016/j.jallcom.2017.02.147

Mbilo, M., Manyali, G. S., & Musembi, R. J. (2022). Ab initio study of K3Cu3P2 material for photovoltaic applications. *Computational Condensed Matter*, ***32***(July). https://doi.org/10.1016/j.cocom.2022.e00726

Meloni, S., Palermo, G., Ashari-Astani, N., Grätzel, M., & Rothlisberger, U. (2016). Valence and conduction band tuning in halide perovskites for solar cell applications. *Journal of Materials Chemistry A*, ***4***(41), 15997–16002. https://doi.org/10.1039/c6ta04949d

Musembi, R., & Mbilo, M. (2022). Ab Initio Study of Structural, Electronic, Elastic, Mechanical, and Optical Properties of K4XP2 (X = Zn, Cd) Compounds for Optoelectronic Applications. *Materialia*, ***26***(June), 101587. https://doi.org/10.1016/j.mtla.2022.101587

Perdew, J. P., & Yue, W. (1986). Accurate and simple density functional for the electronic exchange energy: Generalized gradient approximation. *Physical Review B*, ***33***(12), 8800–8802. https://doi.org/10.1103/PhysRevB.33.8800

Pranab Das. (2022). *Density Functional Theory using Quantum Espresso*.

Ranasinghe, D. S., Perera, A., & Bartlett, R. J. (2017). A note on the accuracy of KS-DFT densities. *Journal of Chemical Physics*, ***147***(20). https://doi.org/10.1063/1.5001939

Shil, S. K., Wang, F., Lai, Z., Meng, Y., Wang, Y., Zhao, D., Hossain, M. K., Egbo, K. O., Wang, Y., Yu, K. M., & Ho, J. C. (2021). Crystalline all-inorganic lead-free Cs3Sb2I9 perovskite microplates with ultra-fast photoconductive response and robust thermal stability. *Nano Research*, ***14***(11), 4116–4124. https://doi.org/10.1007/s12274-021-3351-x

Sholl, D. S., & Steckel, J. A. (2009a). Density Functional Theory: A Practical Introduction. In *Density Functional Theory: A Practical Introduction*. https://doi.org/10.1002/9780470447710

Sholl, D. S., & Steckel, J. A. (2009b). *DENSITY FUNCTIONAL THEORY A Practical Introduction*.

Singh, R. K., Kumar, R., Jain, N., Dash, S. R., Singh, J., & Srivastava, A. (2019). Investigation of optical and dielectric properties of $CsPbI_3$ inorganic lead iodide perovskite thin film. *Journal of the Taiwan Institute of Chemical Engineers*, ***96***(2019), 538–542. https://doi.org/10.1016/j.jtice.2018.11.001

Tao, S., Schmidt, I., Brocks, G., Jiang, J., Tranca, I., Meerholz, K., & Olthof, S. (2019). Absolute energy level positions in tin- and lead-based halide perovskites. *Nature Communications*, ***10***(1). https://doi.org/10.1038/s41467-019-10468-7

Wang, K., Jin, Z., Liang, L., Bian, H., Bai, D., Wang, H., Zhang, J., Wang, Q., & Shengzhong, L. (2018). All-inorganic cesium lead iodide perovskite solar cells with stabilized efficiency beyond 15%. *Nature Communications*, ***9***(1). https://doi.org/10.1038/s41467-018-06915-6

Wu, M., Haji Ladi, N., Yi, Z., Li, H., Shen, Y., & Wang, M. (2020). Stability Issue of Perovskite Solar Cells under Real-World Operating Conditions. In *Energy Technology* (Vol. **8**, Issue 4). Wiley-VCH Verlag. https://doi.org/10.1002/ente.201900744

Yuan, J., Hazarika, A., Zhao, Q., Ling, X., Moot, T., Ma, W., & Luther, J. M. (2020). Metal Halide Perovskites in Quantum Dot Solar Cells: Progress and Prospects. In *Joule* (Vol. **4**, Issue 6, pp. 1160–1185). Cell Press. https://doi.org/10.1016/j.joule.2020.04.006

Zhang, C., Wan, Q., Ono, L. K., Liu, Y., Zheng, W., Zhang, Q., Liu, M., Kong, L., Li, L., & Qi, Y. (2021). Narrow-Band Violet-Light-Emitting Diodes Based on Stable Cesium Lead Chloride Perovskite Nanocrystals. *ACS Energy Letters*, ***6***(10), 3545–3554. https://doi.org/10.1021/acsenergylett.1c01380